Signal Processing Methods and Collision Situation Prediction Using Sensory Systems Based on Fiber Bragg Gratings

Metody zpracování signálu a predikce kolizních situací pomocí senzorických systémů založených na vláknových Braggovských mřížkách

Master's Thesis

Bc. Radek Nesnídal

May 23, 2024

Programme: Electronics and Communications
Specialization: Photonics
Supervisor: doc. Ing. Matěj Komanec, Ph.D.
Consultant: Carlos Guerra Yanez M.Eng.

Department of Electromagnetic Field,
Faculty of Electrical Engineering,
Czech Technical University in Prague

MASTER'S THESIS ASSIGNMENT

I. Personal and study details

Student's name:	**Nesnídal Radek**
Personal ID number:	**491837**
Faculty / Institute:	**Faculty of Electrical Engineering**
Department / Institute:	**Department of Electromagnetic Field**
Study program:	**Electronics and Communications**
Specialisation:	**Photonics**

II. Master's thesis details

Master's thesis title in English:

Signal Processing Methods and Collision Situation Prediction Using Sensory Systems Based on Fiber Bragg Gratings

Master's thesis title in Czech:

Metody zpracování signálu a predikce kolizních situací pomocí senzorických systém   založených na vláknových Braggovských m ížkách

Guidelines:

The goal of the thesis will be a state-of-the-art summary, a theoretical study, data processing, design and experimental verification of a sensor system based on fiber Bragg gratings (FBGs) for monitoring of complex force effects on a given area (e.g. a slope).
In the framework of the thesis focus on these particular goals:
1) Summarize the state of the art on the topic of FBGs.
2) Discuss data processing methods for FBG-based sensor systems.
3) Discuss ambient effects on FBG-based sensor systems (mainly temperature) and propose counter-measures to achieve stable FBG response.
4) Propose approaches to the prediction of FBG-based sensor system behavior with the focus on possible collision states.
5) Propose the topology of the FBG-based sensor system for the detection of selected collision states.
6) Experimentally verify a chosen topology based on 5)
7) Evaluate experimental results and compare them with the prediction.
The outcome of the diploma thesis will be an FBG-based sensor system for collision state monitoring with the prediction capability.

Bibliography / sources:

[1] D. J. Webb, Fibre Bragg grating sensors, p ednáška, COST Summer school 2012
[2] Ch. V. N. Bhaskar, S. Pal, P. K. Pattnaik, Recent advancements in fiber Bragg gratings based temperature and strain measurement, Results in Optics, Volume 5, 2021,

Name and workplace of master's thesis supervisor:

doc. Ing. Mat j Komanec, Ph.D.   Department of Electromagnetic Field FEE

Name and workplace of second master's thesis supervisor or consultant:

Ing. Carlos Guerra Yanez   Department of Electromagnetic Field FEE

Date of master's thesis assignment: **07.02.2024**   Deadline for master's thesis submission: _____

Assignment valid until: **21.09.2025**

_____
doc. Ing. Mat j Komanec, Ph.D.
Supervisor's signature

_____
Head of department's signature

_____
prof. Mgr. Petr Páta, Ph.D.
Dean's signature

III. Assignment receipt

The student acknowledges that the master's thesis is an individual work. The student must produce his thesis without the assistance of others, with the exception of provided consultations. Within the master's thesis, the author must state the names of consultants and include a list of references.

_____._____   _____
Date of assignment receipt   Student's signature

Abstract

Early-warning systems for landslides are essential for the protection of people or structures nearby. Fiber Bragg gratings (FBGs) present a suitable sensor for use in such scenarios due to their extreme sensitivity to strain, their low cost, and their easy deployment. Here, I present an FBG sensor network for slope collision state monitoring, using composite-embedded FBGs. I propose an FBG sensing network topology and data processing techniques. Then, I carry out FBG sensor pilot measurements leading to embedding of FBG sensors into composite material. The experimental campaign then includes landslide simulation and long-term monitoring of an artificial slope with controlled rainfall conditions. Artificial neural networks are used to predict the signal obtained from long-term measurements with a test set root mean squared error of 0.4 pm and a mean absolute error of 0.17 pm.

Key words – Fiber Bragg Gratings, Sensor Networks, Structural Health Monitoring, Early-warning Systems, Artificial Neural Networks

Abstrakt

Systémy včasného varování před sesuvy půdy mají zásadní význam pro ochranu osob nebo staveb v jejich blízkosti. Vláknové Braggovské mřížky (FBG) představují vhodný senzor pro použití v takových scénářích díky své extrémní citlivosti na deformace, nízké ceně a snadnému nasazení. V této práci představuji senzorovou síť založenou na FBG pro monitorování kolizních stavů na svazích pomocí kompozitně zabudovaných FBG. Byla navržena topologie FBG senzorové sítě a techniky zpracování dat. Dále jsem provedl pilotní měření FBG senzorů vedoucí k zabudování FBG senzorů do kompozitního materiálu. Experimentální část pak dále zahrnuje simulaci sesuvu půdy a dlouhodobé sledování umělého svahu s řízenými srážkovými podmínkami. Umělé neuronové sítě jsou použity k predikci signálu získaného z dlouhodobých měření se směrodatnou odchylkou u testovacího datasetu 0,4 pm a střední absolutní chybou 0,17 pm.

Klíčová slova – vláknové Braggovské mřížky, senzorové sítě, monitorování stavu konstrukce, systémy včasné výstrahy, umělé neuronové sítě

Acknowledgement

Declaration

Prohlašuji, že jsem předloženou práci vypracoval samostatně a že jsem uvedl veškeré použité informační zdroje v souladu s Metodickým pokynem o dodržování etických principů při přípravě vysokoškolských závěrečných prací.

I declare that the presented work was developed independently and that I have listed all sources of information used within it in accordance with the methodical instructions for observing the ethical principles in the preparation of university thesis.

In Prague, May 23, 2024

Contents

Chapter 1

Introduction

Fiber-optic technologies have become enormously popular during the last few decades exploiting the unique properties and affordability of optical fibers. Fiber-optic applications range from telecommunications, laser, and high-power delivery to sensing. Among the most widely used fiber-optic sensing technologies are *fiber Bragg gratings* (FBGs).

FBGs allow to selectively reflect a certain wavelength, while the rest is transmitted. This phenomenon is widely used for telecommunication purposes, such as wavelength division multiplexing [1]. In sensing, the FBG sensitivity of reflected wavelength to external phenomena such as temperature and strain have made them very popular in various sensing applications [2]. Structural health monitoring (SHM) is, for example, one of the key applications of FBG sensors.

Currently, high-speed railways are being constructed worldwide and highway networks are constantly expanding, with the nearby slopes being usually more susceptible to landslides. Therefore, there is a request for human safety and mitigation of material damage. Early warning systems should be able to monitor the forces within a slope, so that an alarm could be sent off when approaching a collision state and therefore ensure landslide prevention.

In this thesis, I focus on the application of FBGs for landslide collision state prediction and slope monitoring. Compared to previous published results, I design the monitoring system only to detect movement/stress in the upper slope layer. I also study the signal processing approaches and present prediction routines.

In Chapter 2 I present the state-of-the-art FBG overview, and in Chapter 3 I discuss the signal processing approaches for FBG sensor networks. In Chapter 4 I discuss the setups for slope monitoring, which are then used in the measurements in Chapter 5. The deployment of signal processing and prediction techniques is presented in Chapter 6.

Chapter 2

Fiber Bragg Gratings

FBGs can be seen as a case of a 1D photonic crystal (PhC), whose structure is presented in Figure 2.1. 1D PhC consists of periodic series of layers with different refraction indices in the direction parallel to the direction of guided light. These changes cause reflection of certain wavelengths that depend on the layout of these layers [3].
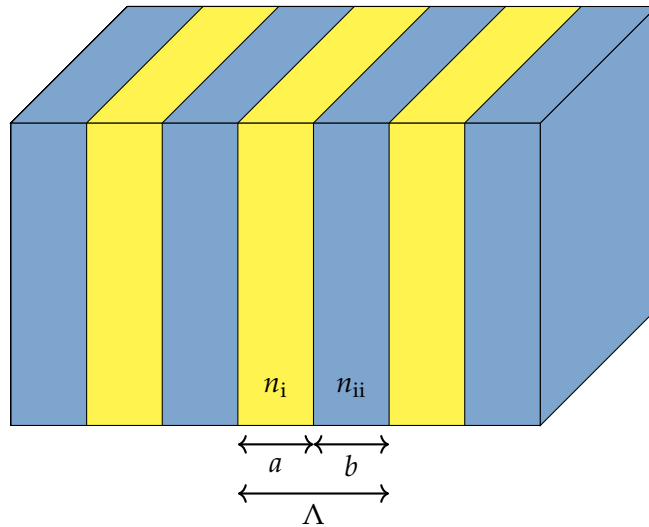

Figure 2.1: Structure of a 1D PhC consisting of layers with different refraction indices.

The calculation of the central wavelength λ_0 in a 1D PhC is presented in [4], where knowing the refraction indices of the grated (n_i) and non-grated parts (n_ii), together with their thicknesses a and b respectively, we are able to calculate the central wavelength as

$$\lambda_0 = 2\frac{n_\text{i}a + n_\text{ii}b}{m} \ , \ m = 1, 2, 3...$$
(2.1)

where *m* represents the order of the Bragg reflection. This equation provides a general way to calculate the Bragg wavelength of FBGs with any type of grating [4].

However, such calculation as the one presented in equation (2.1), provides only an approximate value for the real single mode FBG, as the light guidance in an optical fiber occurs not only within its core but also partially in its cladding part, where the gratings are not present. The incident light is then partially reflected on each grating interface that is present within the core of the fiber, while a small part is still being transmitted through the cladding [2].

The superposition of the reflected light leads to constructive interference near a central wavelength λ_0, while other reflected wavelengths will be out of phase and therefore attenuated compared to the Bragg wavelength [5].

Figure 2.2 presents three cases of superposition of waves with different phase shifts, showcasing the interferometric principle behind the FBG. The top graph shows the case for the Bragg wavelength, where we obtain constructive interference, as the FBG has been designed for such a wavelength. The middle one presents interference of two waves with a phase shift of $\pi/2$, which causes attenuation of the resultant wave compared to the one in the first graph. The last graph represents the scenario during which the two waves have a phase shift π. This causes destructive interference, where the resultant wave is canceled out and therefore no light is being propagated.
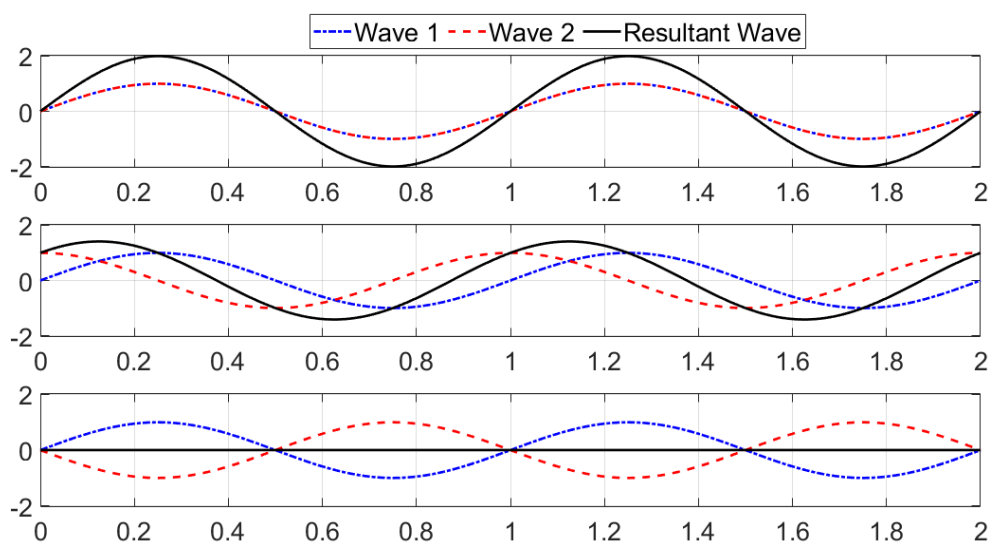

Figure 2.2: An visual interpretation of interference of two waves. Each graph showcases different phase shifts from top − 0, $\pi/2$ and π.

4

In real FBG we, however, have way more waves that are in a superposition, as the number of reflected waves is dependent on the number of gratings. This causes the constructive interference to be way stronger compared to the waves with imperfect phase match, as for wavelengths different to the Bragg wavelength we obtain superposition of multiple waves with various phases [5].

In practice, we can encounter various types of FBGs with different gratings. The most common types are presented below.

Uniform Grating FBGs

The most common type of FBG is its uniformly spaced form, where the thicknesses of grated and non-grated parts are equally wide $a = b$, which corresponds to the spacing being $\Lambda = 2a$. Moreover, all the gratings have the same refraction index of n_1, with the refraction index of the core being n_{core} and the cladding n_{clad}. Knowing these parameters, the Bragg wavelength is then calculated as

$$\lambda_0 = 2n_{\text{eff}}\Lambda, \tag{2.2}$$

where n_{eff} denotes the effective refractive index [2].
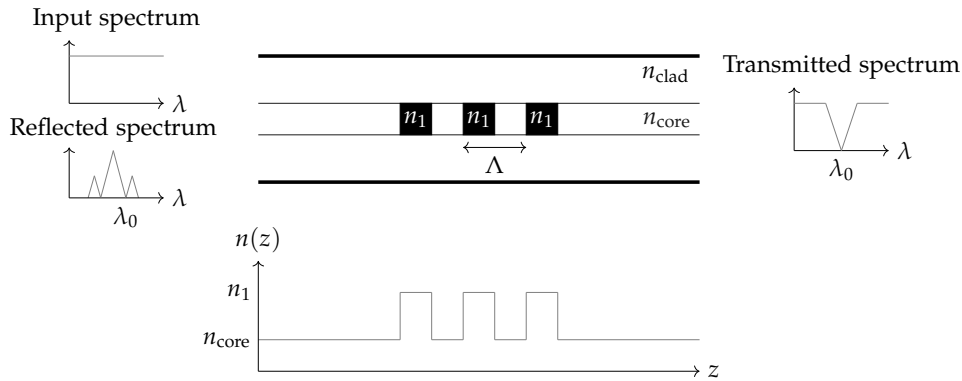

Figure 2.3: The structure and working principle of uniformly grated FBG.

FBGs with non-uniform grating are also very popular, as we can benefit from their properties in some applications. Among the most popular ones are FBGs with apodized and chirped grating profiles [5],[6].

Apodized FBGs

The apodized FBGs have different refraction indices for its gratings, where the strength of the index modulation is maximal in the center of the FBG and gets lower in directions toward the edges. This results into lower reflection of wavelengths at the edges of the spectrum, yielding a spectrum with suppressed side lobes [6]. Figure 2.4 shows the working principle of such FBG.
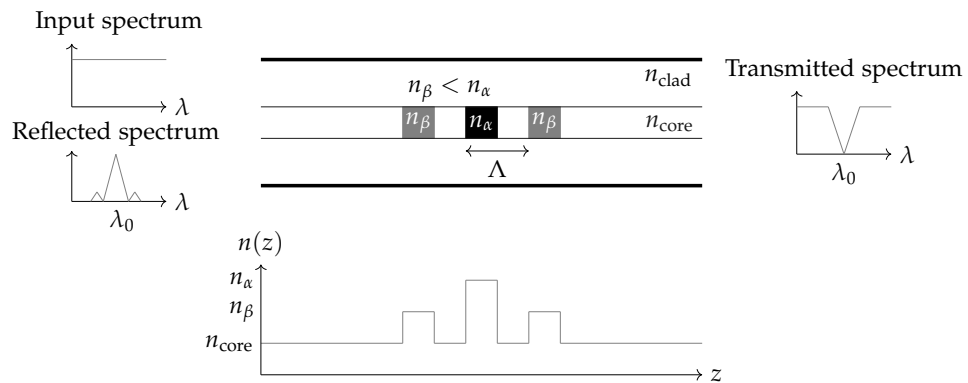
Figure 2.4: The working principle of apodized FBG

Chirped FBGs

The FBGs with chirped gratings are useful in applications where we want to reflect a broadband of the spectrum. This is possible because the spacing among the gratings changes in the fiber. While the fast-changing gratings are responsible for reflecting shorter wavelengths, as the spacing increases, longer wavelengths are reflected [5],[6]. The structure and functionality of the chirped FBG is shown in Figure 2.5.
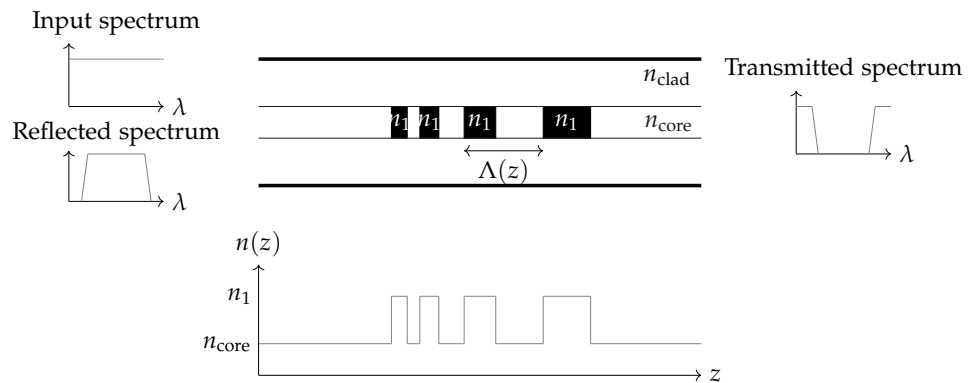
Figure 2.5: The working principle of chirped FBG.

2.1 Response of FBGs to External Phenomena

As mentioned in [2], for FBG sensing applications we use the shift of the refracted wavelength as the parameter that carries the information about the affecting external phenomena. In order to cause such shift of the Bragg wavelength, we need to induce a change in the structure of the FBG, so that n_{eff} or Λ (or both) are affected. Considering equation (2.2), the response can then be derived as

$$\frac{\mathrm{d}\lambda_0}{\mathrm{d}\zeta} = 2\frac{\mathrm{d}(\Lambda n_{\text{eff}})}{\mathrm{d}\zeta} = 2\Lambda\frac{\mathrm{d}n_{\text{eff}}}{\mathrm{d}\zeta} + 2n_{\text{eff}}\frac{\mathrm{d}\Lambda}{\mathrm{d}\zeta}, \tag{2.3}$$

where ζ denotes the affecting external phenomenon. We can further adjust this equation by division by $2n_{\text{eff}}\Lambda$, which together form the Bragg wavelength λ_0. This then yields the following equation

$$\frac{1}{\lambda_0}\frac{\mathrm{d}\lambda_0}{\mathrm{d}\zeta} = \frac{1}{n_{\text{eff}}}\frac{\partial n_{\text{eff}}}{\partial\zeta} + \frac{1}{\Lambda}\frac{\partial\Lambda}{\partial\zeta}. \tag{2.4}$$

For SHM purposes, we are mostly concerned with two phenomena – *strain* and *temperature*. Both of these influences are responsible for changes in the glass material causing a shift in the wavelength of the reflected light [6].

Although strain is the parameter we are most concerned with in SHM, the presence of even slight temperature changes can make precise detection of strain very difficult. Therefore, it is necessary to introduce a temperature compensation of the signal, filtering out the unwanted effect of temperature changes, after which we can observe only the changes that are caused by the applied strain [7].

The parameter values of a silica fiber with significance for SHM purposes are presented in Table 2.1.

Table 2.1: Physical parameters of silica FBGs. Values taken from [2].

Parameter	Value	Units
Maximum continuous service temperature	950	$^\circ$C
Thermo-optical coefficient	$1.19\ 10^{-6}$	$^\circ$C^{-1}
Coefficient of thermal expansion	$5.5\ 10^{-7}$	$^\circ$C^{-1}
Tensile strength	110	MPa
Compressive strength	690–1380	MPa
Young's modulus of elasticity	73	GPa

Strain

The effect of strain being applied on the FBG can be derived considering the equation

$$\frac{1}{\lambda_0}\frac{d\lambda_0}{d\varepsilon} = \frac{1}{n_{\text{eff}}}\frac{\partial n_{\text{eff}}}{\partial\varepsilon} + \frac{1}{\Lambda}\frac{\partial n_{\text{eff}}}{\partial\Lambda}, \tag{2.5}$$

which represents the equation (2.4), where strain is the affecting external phenomenon. As presented in [7], the right side of the equation can be approximated by using the photoelastic coefficient p_ε as

$$\frac{1}{\lambda_0}\frac{d\lambda_0}{d\varepsilon} \approx 1 - p_\varepsilon. \tag{2.6}$$

The value of ε corresponds to the applied strain. It is assumed that the doping of the silica fiber by other elements is negligible, and thus we can use the value of $p_\varepsilon = 0.21$, which is specific for pure silica. This then gives us the final equation of

$$\frac{1}{\lambda_0}\frac{d\lambda_0}{d\varepsilon} \approx 0.79, \tag{2.7}$$

denoting the change of Bragg wavelength with applied strain $\varepsilon = \Delta L/L$, which tells us how the length of the fiber changes compared to its original state, with its dimensionless unit being microstrains, denoting the stretching of the fiber by a one-millionth of its original length.

Force

During measurements, we sometimes prefer to work with the applied force or weight rather than with strain. As mentioned in [8], the relationship between the strain and the applied force is given by following equation

$$\varepsilon = \frac{F}{E\,A}, \tag{2.8}$$

where E denotes the value of Young's modulus (see Table 2.1) and the area of actuation is $A = 125\ \mu$m for conventional silica fiber. The relationship between the weight and the applied force is defined by Newton's second law, as $F = mg$, given that the weight is suspended to one end of a hanging fiber. This relationship between strain and mass is then defined as

$$\varepsilon/m = 11.0. \tag{2.9}$$

This can then be used to define the response of FBG to suspended weight m as

$$\frac{1}{\lambda_0}\frac{d\lambda_0}{dm} \approx 8.57. \tag{2.10}$$

Temperature

Considering the equation (2.4), the response of FBG to changes in temperature is expressed as

$$\frac{1}{\lambda_0}\frac{\mathrm{d}\lambda_0}{\mathrm{d}T} = 2\Lambda\frac{\partial n_{\mathrm{eff}}}{\partial T} + 2n_{\mathrm{eff}}\frac{\partial\Lambda}{\partial T}. \tag{2.11}$$

Both n_{eff} and Λ are temperature dependent, where both dependencies can be approximated with coefficients α_n and α_Λ, which represent the thermo-optical and the thermal expansion coefficient, respectively.

Recalling the values of these coefficients from Table 2.1, of the two, the more significant is the thermo-optical coefficient mainly contributing to the wavelength shift. Considering the values of these coefficients, the equation is then simplified to

$$\frac{1}{\lambda_0}\frac{\mathrm{d}\lambda_0}{\mathrm{d}T} = 6.678, \tag{2.12}$$

which means that for most commonly used wavelengths around 1550 nm we get response of 10.35 pm/°C [9],[7].

2.2 Manufacturing of an FBG

Various techniques were developed for the fabrication process of the FBGs, with some of the most popular ones are presented in this section. These methods usually take advantage of the photosensitivity of silica fiber, due to which we can alter the inner properties of the silica fiber and thus inscribe the gratings to the core of the fiber [2].

Interferometric Method

These methods use the properties of interferometry, which were described at the beginning of this chapter, to induce changes in parts of a fiber to fabricate an FBG. As shown in Figure 2.6, a UV light beam is split into two parts using a beam splitter. Each beam is then reflected from a mirror, where the reflection is pointed towards the fiber. Depending on the angle φ between the two incident beams, a given interference pattern occurs, inscribing the grating with a corresponding Bragg wavelength λ_0 according to equation

$$\lambda_0 = \frac{n_{\mathrm{eff}}\ \lambda_{\mathrm{UV}}}{n_{\mathrm{UV}}\ \sin\left(\varphi/2\right)}, \tag{2.13}$$

where λ_{UV} denotes the wavelength of the incident UV light and n_{UV} presents the refraction index of the silica fiber at this wavelength [2]. The disadvantage of this technique lies in the difficult alignment of the beams or in the fact that we need to ensure a stable environment. The reason for this is that air flow can affect the air refraction index, which could lead to distortion of the beam wave front, leading to the fabrication of poor quality FBGs [10].
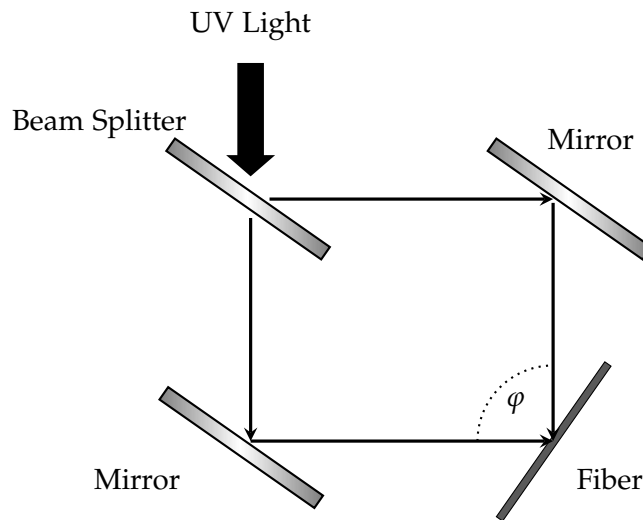
Figure 2.6: Manufacturing of an FBG by inscribing gratings to a silica fiber using interferometric technique, where interferometric patter occurs due to a superposition of two incident beams. Inspired by [2].

Phase Mask

Phase mask method presents one of the most popular techniques for FBG manufacturing. Figure 2.7 presents the working principle of such fabrication method.
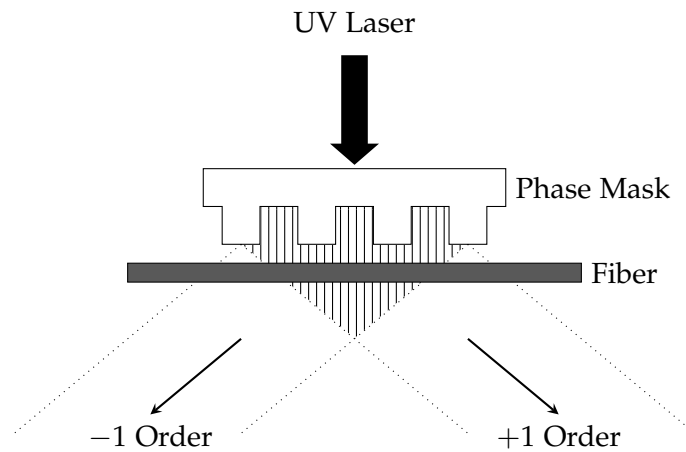

Figure 2.7: Illustration of the fabrication process of an FBG with the use of a phase mask, showcasing how ±1 order diffraction beams cause interference in the near field by the phase mask. The fiber is then inserted there to inscribe the grating to its core. Inspired by [10].

As presented in [10], during this fabrication of the FBG a phase masks is used for spatial modulation of an ultraviolet (UV) beam with a period of Λ_{pm},

where diffraction of the laser light causes division of the beam into multiple orders. The zero order is then suppressed, causing the ± 1 orders to retain most of the power. These orders have the same starting point but different divergence, which causes interference pattern to occur only in the near field. The fiber is then placed within the near field, where the light inscribes the gratings within its core at positions corresponding to the interference pattern. The grating period of the FBG Λ is then given by the equation

$$\Lambda = \Lambda_{\mathrm{pm}}/2. \tag{2.14}$$

Point by Point Writing

Another approach for FBG manufacturing consists of writing each grating one at a time. Therefore, instead of taking advantage of the interferometric pattern, here a setup consisting of a lens that focuses a laser beam to a point of interest is used.

The working principle also does not rely on the photosensitivity of the fiber, as femtosecond lasers are used for the interaction with the dielectric material via non-linear photoionization mechanisms. Mechanisms like multiphoton and tunnelling ionization are then used for the direct inscription. The Bragg wavelength of the FBG is then defined as

$$\lambda_0 = \frac{2n_{\mathrm{eff}}v}{mf}, \tag{2.15}$$

where m represents the order of the grating, v denotes the velocity of the translation stage pulling the fiber and f is the pulse repetition of the laser [11].
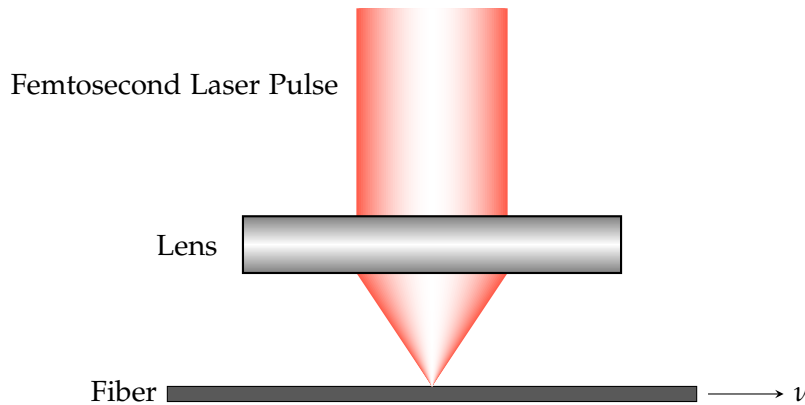

Figure 2.8: Demonstration of the point-by-point manufacturing process, where each grating is individually inscribed to a fiber that is being pulled at velocity v.

The techniques demonstrated in this section show that there are many ways to manipulate the spacing of the inscribed grating during the manufacturing processes, and we can obtain FBGs with many different wavelengths. In fact, this is essential for FBG sensor networks, which are presented in the following section.

2.3 FBG Sensor Networks

Sensor networks enable the deployment of multiple sensors simultaneously, allowing complex measurements of various phenomena at the same time. As presented in [12], a typical FBG-based sensor network consists of the following components

- Light source

- 1 to N channels optical switch

- Multiple FBGs

- Optical spectral analyzer (OSA) or FBG interrogator.

With such components, we are able to set up a network capable of periodic measurements of the Bragg wavelength at all FBGs that are within the network.

The most common way of detecting wavelengths reflected by an FBG is by using an OSA. OSAs usually use prisms or gratings to divide the wavelengths, which are then detected by a photodetector [1]. However, the use of conventional OSAs is not suitable for FBG sensing applications, where we aim for a much higher spectral resolution compared to the one that OSAs typically provide. For reference we can take commercially available OSA AQ6370E from Yokogawa[1] with spectral resolution of 0.02 nm. For that reason, interrogation techniques were developed for better spectral resolution [6].

Most commonly, interrogation techniques use a laser as a light source to scan through a band of wavelengths. In such a setup, a single photodetector is used for the measurement of the current power of the reflected light by the FBG at the wavelength given by the wavelength of the laser. The spectral resolution is determined by the step of the laser scan, which is limited by the linewidth of the laser spectrum [12]. This is showcased in Figure 2.9, where three acquired spectra are presented, with the laser steps of the interrogator being 5 pm, 78 pm, and 156 pm.

2.3.1 Network Topology

In general, we can consider two possibilities on how to divide sensor networks based on the way the FBGs are connected. One way is to connect FBGs in parallel, which provides us a significant advantage of not having an overlap among the FBG wavelength spectra, as they are all connected independently. This means that we will use time division multiplex (TDM), during which

---

[1]https://tmi.yokogawa.com/solutions/products/optical-measuring-instruments/optical-spectrum-analyzer/aq6370e-telecom-optical-spectrum-analyzer-600-1700-nm/
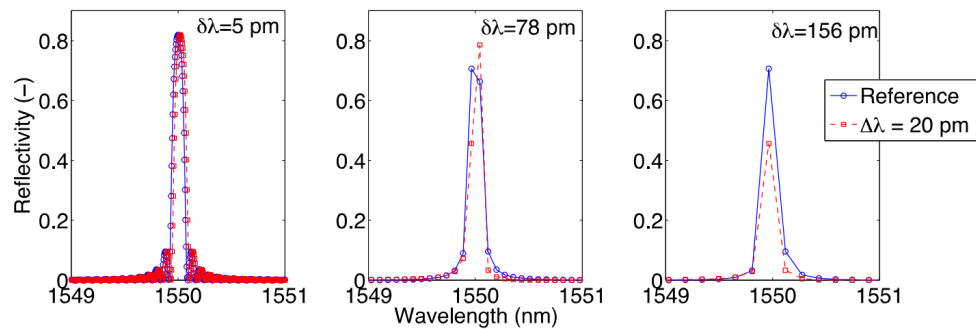
Figure 2.9: Dependence of acquired spectra on the resolution of the laser scan. The graphs contain two 20 pm shifted peaks detected by lasers with various scan resolutions. Adapted from [12].

each channel is read out at different time. However, parallel layout is also an expensive and complex solution, which requires more cabling and a switch unit [9]. The topology of this network is shown in Figure 2.10.
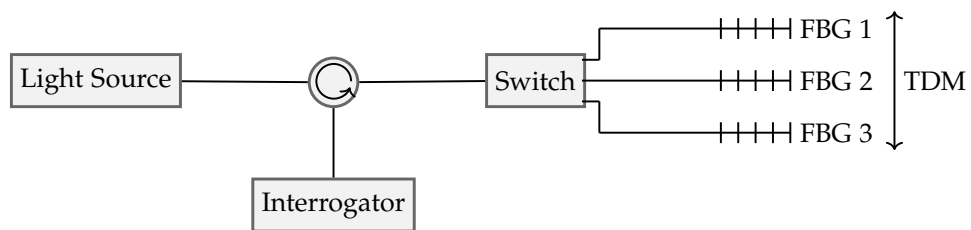

Figure 2.10: Topology of a FBG-based sensor network with parallel connecting.

Layout with FBGs in series is less demanding on resources, without the need for an optical switch. This approach is possible due to differently manufactured FBGs that operate on different wavelengths that do not overlap. However, such a layout needs to be carefully configured, considering the wavelength division multiplex (WDM) spacing, which is generally also limited by the light source and the OSA or interrogator [9],[13]. The topology of this network is presented in Figure 2.11.
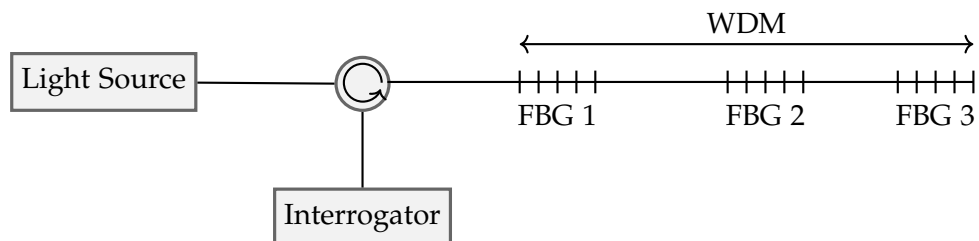

Figure 2.11: Topology of a FBG-based sensor network with serial connections.

We can also merge the serial and parallel connecting, creating a complex sensor network that takes advantage of the benefits of both approaches. Its deployment is shown in Figure 2.12.
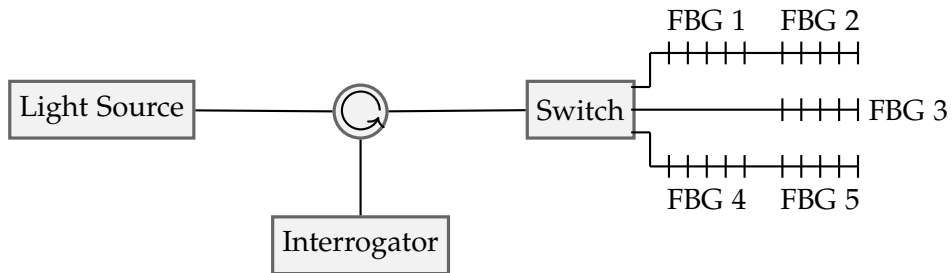

Figure 2.12: Topology of a complex FBG-based sensor network with both parallel and serial connections.

Chapter 3

Data Processing Methods

To extract the desired information from FBG sensors, various signal processing techniques have to be deployed. The successive layers for slope monitoring are presented in Figure 3.1.

Figure 3.1: Signal processing layers regarding FBG sensing for collision state detection.

3.1 Peak Detection

The sensing tasks of FBG sensor networks revolve around the change in the reflected wavelength by the FBG. Therefore, a precise detection of the peak wavelength from the acquired spectrum plays a crucial role in FBG sensing.

3.1.1 Direct Methods

Maximum Method

Having obtained the spectrum with a laser that has a sufficiently narrow linewidth, we can now track the wavelengths of the peaks λ_{peak} reflected by an FBG. The most straightforward method would be to track the detected wavelength λ with the highest power defined by the reflectivity $R(\lambda)$, which can be expressed by the following equation

$$\lambda_{\text{peak}} = \lambda|_{R(\lambda)=\max(R(\lambda))}.$$

(3.1)

This technique is easily implementable but is highly limited by the laser scanning step. For more accurate peak estimation we usually deploy more complex methods [14].

3dB Method

Another commonly used technique is the 3dB method, where we consider all the wavelengths λ_{th} that are within 3dB attenuation compared to the wavelength with the highest reflectivity R_{max}, calculated as

$$\lambda_{th} = \lambda|_{R(\lambda) \geq R_{max} - 3 \text{ dB}}.$$ (3.2)

The peak wavelength is then estimated as the center between the lowest and highest wavelength, calculated as

$$\lambda_{peak} = \min(\lambda_{th}) + \frac{\max(\lambda_{th}) - \min(\lambda_{th})}{2}.$$ (3.3)

Centroid Method

The centroid method provides another way of calculation of the peak wavelength from the acquired spectra. The peak wavelength is computed using the values of the samples of wavelengths λ_n and their corresponding reflectivities $R(\lambda_n)$, as

$$\lambda_{peak} = \frac{\sum_n \lambda_n R(\lambda_n)}{\sum_n R(\lambda_n)}.$$ (3.4)

This method calculates the Bragg wavelength by identifying the center of mass of the FBG's reflection spectrum [12],[14].

3.1.2 Polynomial Fitting Methods

While the direct methods determine the peak directly from the data, fitting techniques use curves to approximate its spectral shape. Among those commonly used techniques is second-order polynomial fitting, which approximates the peak using following equation

$$R(\lambda) \approx a_2\lambda^2 + a_1\lambda + a_0.$$ (3.5)

To find the peak of such a function, we have to set its first derivative to zero $dR/d\lambda = 0$, which yields

$$2a_2\lambda + a_1 = 0.$$ (3.6)

From here we can adjust the equation and acquire following equation for peak determination as

$$\lambda_{peak} = -\frac{a_1}{2a_2}.$$ (3.7)

The coefficients a_0, a_1, and a_2 are obtained by least-squares interpolation based on quadratic regression. For such calculations, we only work with the part of the spectrum that resembles the shape of a quadratic function. This is done through thresholding such as the one presented in equation (3.2),

where only the wavelengths within the attenuation limit of $3\,\mathrm{dB}$ (or other based on application) that contain the peak are considered [12]

Another popular method is the *Gaussian fitting*, where we approximate the FBG spectrum as

$$R(\lambda) \approx A \exp\left[-\frac{(\lambda - \lambda_0)^2}{2\sigma_{\mathrm{Gauss}}^2}\right], \tag{3.8}$$

where A denotes the amplitude, σ_{Gauss} is the standard deviation and λ_0 presents the peak wavelength. As shown in [12], after adjusting the equation with similar steps as presented for second-order polynomial fit, we again obtain equation for calculation of the Bragg wavelength as

$$\lambda_{\mathrm{peak}} = -\frac{a_1}{2a_2}. \tag{3.9}$$

The Gaussian fit is then approximated through a second-order polynomial fit, where the coefficients a_0, a_1, and a_2 are functions of the Gaussian parameters A, σ_{Gauss}, and λ_0. It is also possible to perform Gaussian fitting by applying the least squares method to the spectrum yielded by equation (3.8), where the the desired parameter to be estimated being λ_0.

3.2 Artificial Neural Networks

Artificial neural networks (ANNs) present artificial intelligence methods that are inspired by the functionality of the neural network of the human brain. Unlike conventional machine learning methods, such as logistic regression, support vector machines, or decision trees, ANNs have the ability to learn from data without the need for a priori hand-crafted features and rather extract them themselves through their training [15]. ANNs learn to represent the data with multiple abstraction levels, which then enables ANNs to learn to represent complex functions or perform classification tasks [16]. ANNs therefore present a suitable method for complex signal predicting tasks.

As mentioned in [17], the working principle of ANNs typically revolves around the *perceptron* (shown in Figure 3.2). Perceptrons transform the incoming inputs x_{n} that together form a vector $\mathbf{x}$, by multiplication with their corresponding weights w_{n} of vector $\mathbf{w}$. The products of each weight w_n and their corresponding input x_n are summed together, along with the bias value b, producing a scalar z. Mathematically this can be expressed using following equation

$$z = \mathbf{w}^{\mathrm{T}}\mathbf{x} + b. \tag{3.10}$$

The product z is an input variable of an activation function f, yielding an output of the perceptron y as
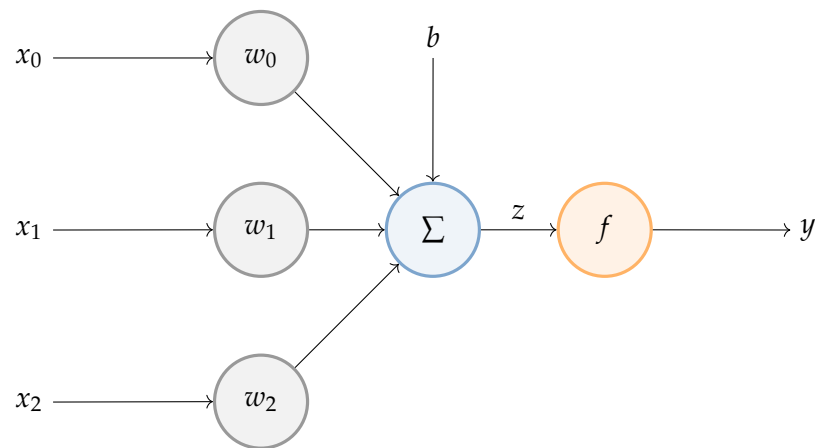
$$y = f(z). \tag{3.11}$$

Figure 3.2: Perceptron – A basic building block used in ANNs.

The choice of the activation function can vary with the layer and the task that we want to perform. Among the most commonly used functions is the rectified linear function (ReLU) defined as $f(z) = max(z, 0)$, hyperbolic tangent $\tanh(z) = \frac{e^z - e^{-z}}{e^z + e^{-z}}$, or sigmoid function $\sigma(z) = \frac{1}{1 + e^{-z}}$ (all presented in Figure 3.3) [15].
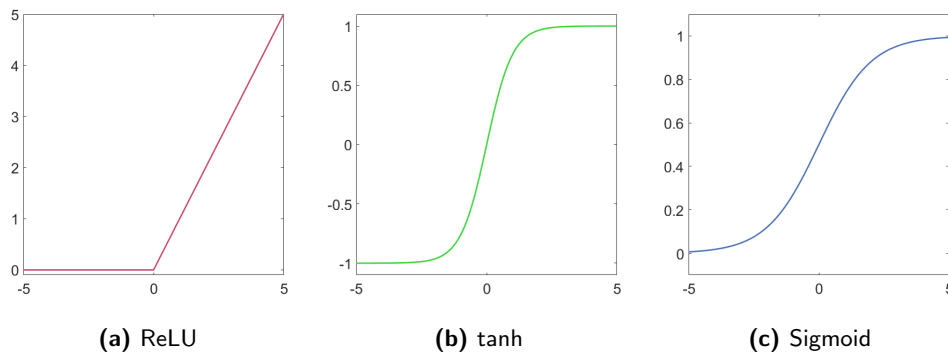

(a) ReLU   (b) tanh   (c) Sigmoid

Figure 3.3: Commonly used activation functions.

Connecting outputs of multiple perceptrons forms a so-called fully connected layer, which is among the most used hidden layers in ANNs. The hidden layers represent all the layers that are between the input and output layers [16].

Figure 3.4 presents a typical ANN, showcasing how the individual nodes are connected to each other. Each node of the output and hidden layers represents one perceptron whose inputs consist either of input data from the input layer or outputs from the previous hidden layer.
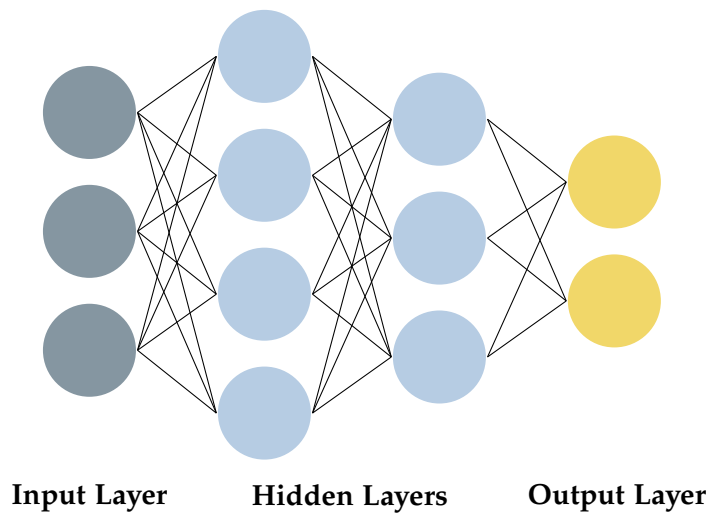
Input Layer   **Hidden Layers**   **Output Layer**

Figure 3.4: Illustrative representation of the layers present of an ANN together with their interconnections.

3.2.1 Training of an ANN

The previously presented structure of ANN is now ready to be trained. This is an essential part of deep learning, as the weights of the neurons are initially set randomly. Such values are most likely not optimal, and therefore we need to adjust them to improve the results.

For the ANN to be capable of learning, we need to introduce a cost function J, which represents a multidimensional error function in whose minimum lies the optimal result – the perfect prediction. The learning task can then be viewed as an optimization problem, with the optimization criterion being the minimization of J [15]. The learning itself is then done through a series of iterative steps known as *backpropagation*. The results obtained during each training epoch by the ANN are compared with the correct values (e.g. the true values of next samples of a signal when comparing prediction by the ANN). Calculating the error derivative, denoting the direction pointing to the minimum of J, the weights and biases within the network are adjusted accordingly [16].

Overall, the learning capability is affected by multiple factors collectively called the *hyperparameters*. The values of these hyperparameters are defined a priori and do not change during the training process [15]. Typical examples are the number of hidden parameters (neurons), the learning rate, the number of layers within the network (also called its depth), or the batch size, denoting the number of samples used for each iteration of the learning epoch.

Stochastic Gradient Descent

Stochastic gradient descent (SGD) presents one of the most widely used techniques for cost function minimization. The optimization problem of gradient descent algorithms is defined by the following equation

$$\min_{\theta} J(\theta) = \min_{\theta} \frac{1}{n} \sum_{i=1}^{n} l_i(g(x_i, \theta), y_i), \qquad (3.12)$$

where l_i represents the loss function for the i-th sample x_i, where $g(x_i, \theta)$ is the output of a node of an ANN with corresponding true value of y_i. The weights and biases of the model are represented by θ and their values collectively determine the value of the cost function. The individual loss functions together add up to the final value of the cost function [18],[15].

During the backpropagation, we update the values of the weights and biases of θ as

$$\theta_{\text{update}} = \theta - \frac{\eta}{n} \sum_{i=1}^{n} \nabla_{\theta}\, l_i(g(x_i, \theta), y_i). \qquad (3.13)$$

The gradient of the loss function l_i provides the direction in which the minimum of the given loss function from the current weights lies. We then take a step in this direction, which is steered by a parameter η called the learning rate. This parameter is set in such a manner that we do not take excessively large steps, which could result in overshooting of the minimum [18].

If we would calculate the values of all loss functions l_i, we could obtain the true value of the gradient. However, SGD calculates the cost function only from randomly selected loss functions, which then provide unbiased estimates of the real gradient [15].

To further evolve on the idea behind SGD, momentum was introduced to speed up the cost function minimization algorithm. Momentum adjusts the gradient vectors so that they are accelerated in the direction towards the minimum of the cost function, when having a limited learning rate, dealing with high curvature of the function, or when we are dealing with small or noisy gradients [15],[18]. The working principle is presented in Figure 3.5.

To further optimize the learning process, the solver called *adaptive moment estimation* (ADAM) was developed, presenting a computationally and memory-efficient method for minimization of a cost function. ADAM uses momentum as previously presented and also an adaptive learning rate, which ensures that we take smaller steps as we get closer to the minimum [19].
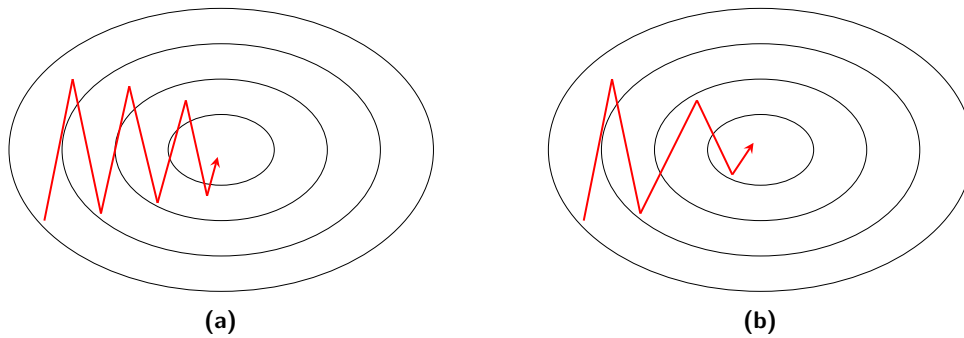
Figure 3.5: The difference between the steps taken during cost function minimization by the SGD without (a) and with (b) the use of momentum. Inspired by [18].

Generalization, Overfitting and Regularization

After the training is completed, we acquire the parameters of our model. Depending on the previously set metric, we know how well it performed on its training dataset. However, the performance of this model on previously never seen data can vary, depending on its *generalization* [15].

A high complexity of a network and too many training epochs can lead to the network picking up on outliers, resulting in *overfitting*. This means that while during the training process the training error got lower, at some point the generalized error started to increase and this model would not be suitable for deployment on new data [17].

The introduction of a validation set can help us identify overfitting during the network training. Validation sets usually consist of fewer samples of the data compared to the training set, and during the training process, the model does not access these data. For each epoch, the ANN is then trained using the available training dataset and afterwards computes how it performs on the validation set. Depending on this performance, we know that if the training loss decreases but the validation one does not, we might be encountering overfitting [15].

There are many ways to prevent overfitting of a network, collectively called *regularization techniques*. Having the validation set available, we can introduce early stopping, which terminates the training process when the validation loss has not been decreasing for given number of epochs (also called the validation patience). In this way, we can ensure that the model remains generalized even during training with a large number of epochs [20].
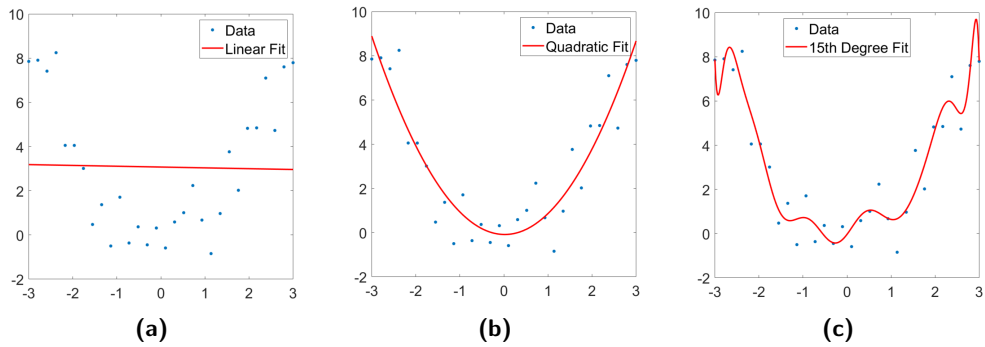
Figure 3.6: Visual representation of overfitting in regression task. The noisy quadratic function has (a) linear, (b) quadratic and (c) 15th degree polynomial fit, resulting in underfitting, optimal fit and overfitting respectively.
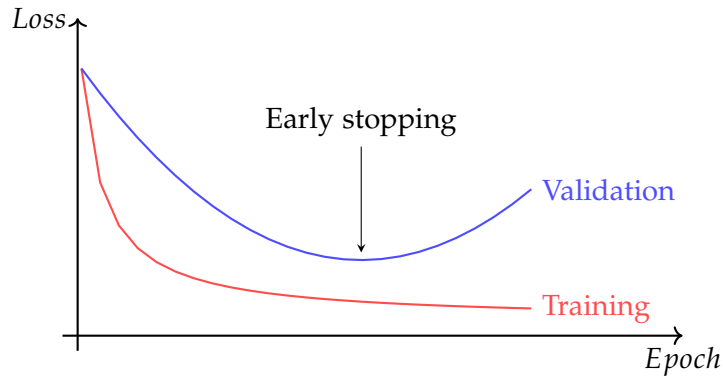

Figure 3.7: Graph showcasing the problematic revolving overfitting during ANN training. Early stopping solves such problem by choosing the model with lowest validation loss rather than the one with lowest training loss.

3.2.2 From Recurrent ANNs to Long Short-Term Memory

Up to this point, only the so-called feedforward-structure ANNs were considered. Such networks have been shown to have limited ability to learn from patterns in previously processed data. Recurrent neural networks (RNNs) were developed to deal with such a problem by introducing an additional input to deal with such problem [21].

Given sequential data $\mathbf{x}^{(t)}$ with t denoting its time step index or epoch, RNNs process such data to compute current values of their hidden units $\mathbf{h}^{(t)}$ as

$$\mathbf{h}^{(t)} = f(\mathbf{h}^{(t-1)}, \mathbf{x}^{(t)}, \theta), \tag{3.14}$$

where θ denotes a vector that holds the current weights and bias values [15]. Figure 3.8 presents the described structure, without outputs, used only to feed the hidden unit to the subsequent epoch.
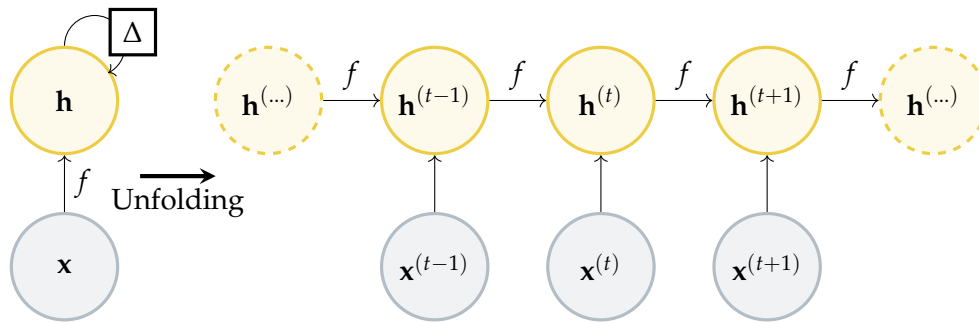
Figure 3.8: Folded and unfolded versions of a RNN. Recurrent behaviour of RNN is presented by showcasing the passing of the hidden state of the previous epoch $\mathbf{h}^{(t-1)}$ to the current epoch state $\mathbf{h}^{(t)}$. Inspired by [15].

The state vector is updated with each iteration, during which we process an input sequence element x^{ξ} at a time, where $\mathbf{h}^{(t)}$ stores information about the already processed elements of the given sequence. As the current values of $\mathbf{h}^{(t)}$ are also a function of the past values $\mathbf{h}^{(t-1)}$, the state vector retains the information about its past. The output of the hidden unit is then used at a given time step t in a similar way, as if an additional input of a neuron was present [16].

Long Short-Term Memory

Long short-term memory (LSTM) cells further evolve on the idea behind RNNs, with the aim of dealing with long-term dependencies [21]. This is possible thanks to the introduction of self-loops to the structure of LSTMs that enable the transition of gradients for a much longer duration compared to conventional RNN, dealing with the so-called vanishing gradient problem [15].
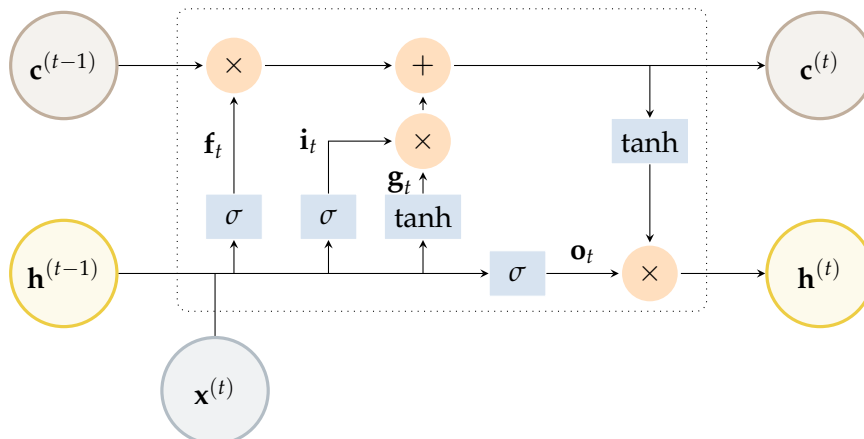
Figure 3.9: The inner structure of a LSTM cell.

Figure 3.9 presents the composition of an LSTM cell. Recalling Figure 3.8, we can see that the forward passing of the hidden unit $\mathbf{h}^{(t)}$ is done in a similar manner to the RNNs. Additionally, a cell state is introduced into the LSTM, where the state of the previous epoch $\mathbf{c}^{(t-1)}$ further influences the inner working of the LSTM cell.

The inner structure of the LSTM consists of gates that perform different tasks and together influence the outputs of the cell. The forward pass of the LSTM cell is defined by the following equation

$$
\begin{pmatrix} \mathbf{f}_t \\ \mathbf{i}_t \\ \mathbf{o}_t \\ \mathbf{g}_t \end{pmatrix} = \begin{pmatrix} \sigma \\ \sigma \\ \sigma \\ \tanh \end{pmatrix} \mathbf{W} \begin{pmatrix} \mathbf{h}_{t-1} \\ \mathbf{x}_t \end{pmatrix}, \tag{3.15}
$$

where t denotes the current time step and σ or tanh are the used activation functions for a given gate. The gates are then calculated by applying their assigned activation functions to a product of the weight matrix $\mathbf{W}$ with the input $\mathbf{x}_t$ and the hidden state $\mathbf{h}_{t-1}$. This yields the values for the forget gate $\mathbf{f}_t$, the input gate $\mathbf{i}_t$, the output gate $\mathbf{o}_t$, and the $\mathbf{g}_t$ used for cell state modification. The current cell state $\mathbf{c}_t$ is then calculated using the following equation

$$
\mathbf{c}_t = \mathbf{f}_t \odot \mathbf{c}_{t-1} + \mathbf{i}_t \odot \mathbf{g}_t, \tag{3.16}
$$

and the hidden state h_t is obtained as

$$
\mathbf{h}_t = \mathbf{o}_t \odot \tanh\left(\mathbf{c}_t\right), \tag{3.17}
$$

where $\odot$ presents element-wise multiplication among the gate outputs [22].

The forget gate presents the first of these gates and is used to determine which samples of the cell state data $\mathbf{c}^{(t-1)}$ to retain [21]. Furthermore, the input and output gates that are subsequent are used to further control the information flow [15].

In ANN signal prediction tasks we usually use both fully connected and LSTM layers to learn from the data, taking advantage of their unique properties.

3.3 Ambient Effect Compensation

During a measurement with FBG sensors, we usually try to detect only one phenomenon (strain or temperature). However, various ambient effects induce changes within the structure of the FBG and therefore result in a parasitic wavelength shift. For precise measurement of the parameter of interest, compensation has to be introduced to discriminate for such effects.

Temperature

In FBG sensing, the most common discrimination technique is temperature compensation. As already presented in the previous chapter, temperature induces changes within the FBG structure resulting in significant wavelength shifts (10.35 pm/°C for peak at wavelength of 1550 nm), hence the need for compensation [6].

The most common temperature compensation is achieved by having a pair of FBGs. One of those FBGs is used for detection of the desired phenomenon (mostly strain), while the second is installed in such a way that this affecting phenomenon does not influence it (e.g. strain free). The temperature discrimination can be then achieved by subtraction of the shift on the temperature-sensing FBG $\Delta\lambda_2$ from the shift of the other FBG $\Delta\lambda_1$, yielding the value of the temperature-compensated shift $\Delta\lambda_{1\,comp}$ as

$$\Delta\lambda_{1\,comp} = \Delta\lambda_1 - \kappa_T \Delta\lambda_2. \tag{3.18}$$

The value of κ_T denotes the temperature sensitivity ratio, which defines the relationship between the shifts of the two FBGs because the temperature change-induced wavelength shift depends on the initial Bragg wavelength [23],[7].

Compensation for temperature changes can also be achieved during strain measurement by having a composite structure with two embedded FBGs. With each of the FBGs placed on opposite sides of the composite, the strain-induced wavelength shift is positive on one of the FBGs, while being negative on the other one. This means that one of the FBG experiences compression within its structure due to the bending, while the curvature at the other end causes the fiber to stretch, hence the opposite shifts. By subtracting the two wavelength shifts we therefore obtain temperature-compensated information about the applied strain [23]. A visual representation of this effect is presented in Figure 3.10.

For deployment in large-scale FBG sensor networks, we usually prefer to use one unaffected FBG that would be used for temperature change sensing. The signal of this FBG would then be used for compensation on multiple FBGs that are within a certain range, where we do not expect significant temperature variations [13].
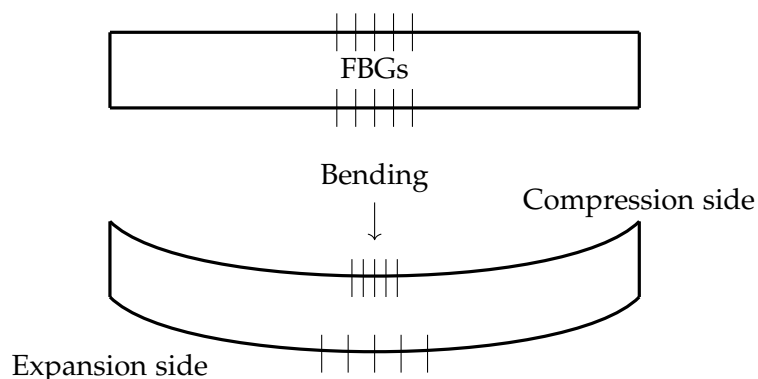
Figure 3.10: Temperature compensation technique utilizing measurement of applied strain. The opposite shifts are present due to the bending of the composite structure, resulting in compression on one side, while inducing expansion on the other side.

Short-Term Variations

Other ambient effects that might disrupt an FBG measurement are short-term variations. FBGs proved to be suitable as a vibration sensor [24], however, when monitoring strain or force within a soil to detect its movement, vibrations could introduce unwanted noise to the detected signal. In SHM such vibrations might be caused by movement near the FBG sensor or by other short-term phenomena that do not affect the properties within the soil, and thus are redundant.

As presented in [25], the moving average (MA) filter presents a suitable method for filtering out short-term fluctuations. The MA filter uses past samples x to determine the value of the currently detected sample $\hat{x}$, as

$$\hat{x}_k = \frac{1}{k} \sum_{i=n-k+1}^{n} x_i, \tag{3.19}$$

where k represents the number of samples that we consider to filter the value of the n-th sample.

There are also noise reduction techniques that do not require additional signal processing, such as the embedding of the FBG in a composite structure such as carbon, as presented in [26]. The surrounding material reduces the amplitude of the vibrations that affect the FBG, resulting in reduced noise in the FBG signal.

Chapter 4

Thesis focus – Landslide Collision State

As presented in Chapter 2, FBGs can be used as a sensor of strain/force and temperature. From this point on, the main focus of this thesis is placed on experiments focused on the landslide monitoring. FBGs present a suitable sensor for such a task due to their relatively low cost, and easy deployment.

My research focused on the detection of movement of the upper 30 cm of the slope. Such landslides occur most commonly near newly constructed highways or railways, where the terrain along these structures was heavily affected. Most of these slopes were built from scratch, thus having the possibility of collapsing.

4.1 State-of-the-Art Approaches to Landslide Detection

Inclinometers

Among the most popular ways to detect slope movements is with FBG-based inclinometers. An inclinometer consists of a bar, usually x meters long, with multiple FBGs embedded within its structure, providing protection and robustness to the FBG sensor [27]. The bar is then inserted vertically into a slope, where the movement of the soil then causes the inclinometer to tilt, affecting the Bragg wavelength reflected on all the FBGs [28].

Figure 4.1 presents the working principle of FBG inclinometers, showing how deflection on one end causes a slight displacement throughout the whole length of the inclinometer. The presented measurement is used for calibration, and we can then assign a given shift of the Bragg wavelength to a certain displacement [29].
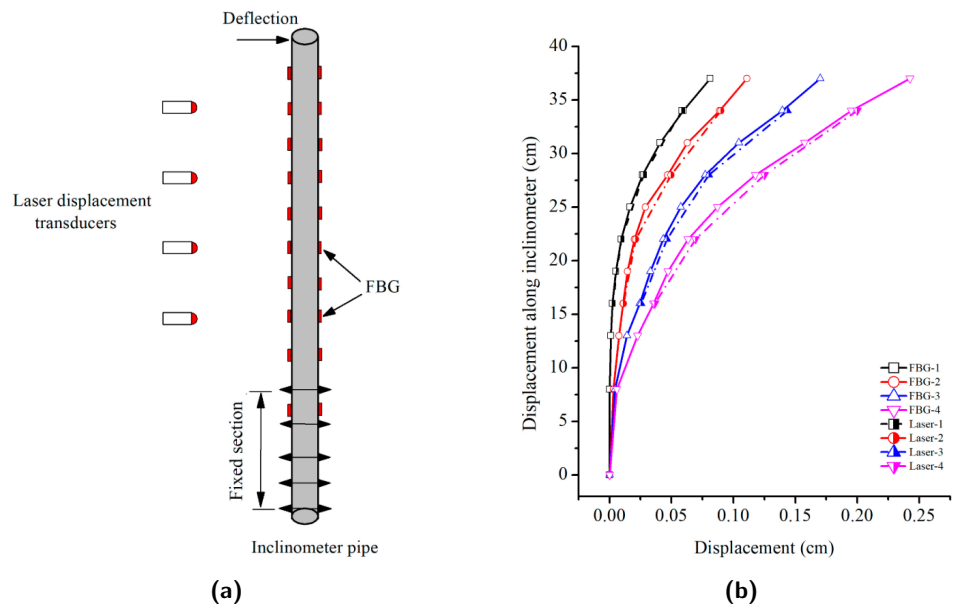
Figure 4.1: Calibration step for an FBG inclinometer (a), where (b) shows the difference between measured displacement and the one obtained by laser displacement transducers. Adapted from [29].
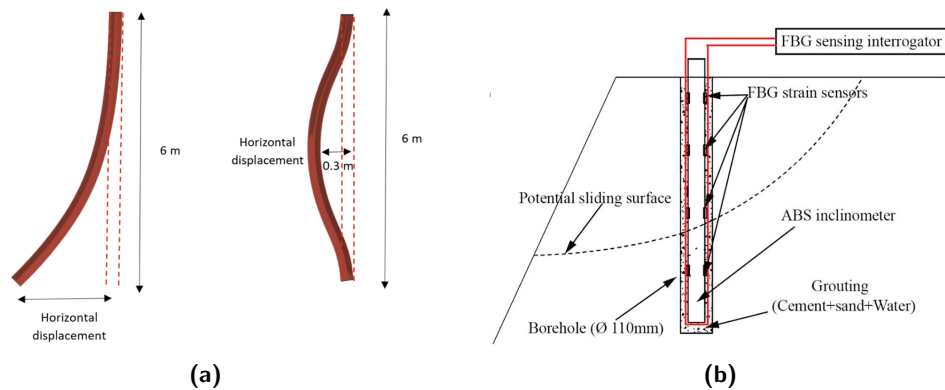
Figure 4.2: The working principle of FBG inclinometer for landslide monitoring, (a) shows how differently positioned force causes different bend of the inclinometer (adapted from [28]), while (b) presents an illustration of the structure of the inclinometer installed within a soil mass (adapted from [30]).

The use of inclinometers has become quite popular recently and this approach is suitable for measurements where we want to track the forces within the soil in various depths. For cases where only research the sliding surface movements, some of the data provided by inclinometers might be redundant.

FBGs Embedding Approaches

An alternative approach for strain measurements using FBGs utilizes their embedding within composite structures. An FBG is placed between one of the layers of the composite and is bound using adhesive. The surrounding composite provides higher strength and stiffness and corrosion resistance to the FBG sensor, improving both the thermal and acoustic properties [31]. Figure 4.3 presents the composition and a real picture of the embedded FBG.

(a)   **(b)**
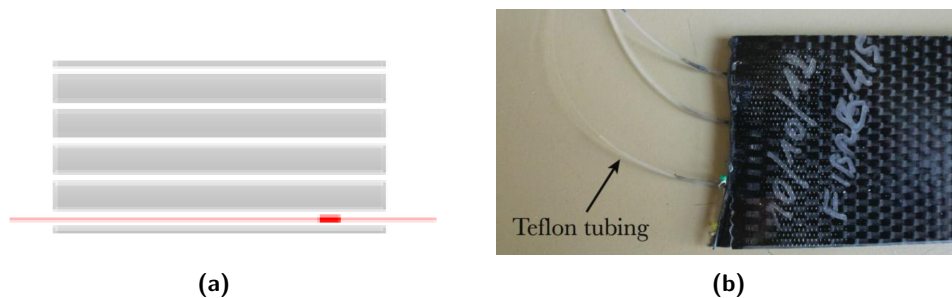
Figure 4.3: The composition of the composite layers with the embedded FBG to a lower layer (a) (adapted from [26]), and an actual composite-embedded FBG with teflon tubing for protection of the fiber leading in (b) (adapted from [7]).

The maximal response to strain can be affected by the choice of placement of the FBGs among the composite layers. Inserting the FBG into a non-centric layer away from the plane of symmetry results in the applied strain having a bigger impact on the FBG. Therefore, in such case we obtain a higher response, compared to a case where FBG would be placed to the central layer of the composite structure [26].

The fiber is fixed within the composite structure in a similar manner to the one presented in Figure 4.4 [23]. All the forces affecting the area of this composite are then being transferred to the FBG.
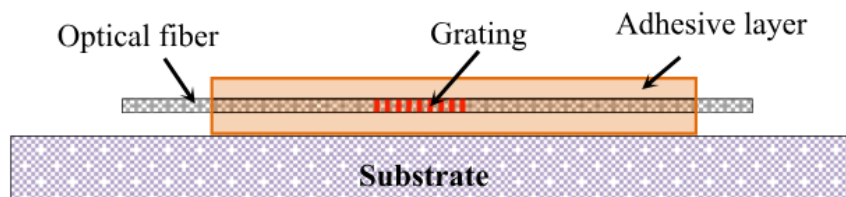
Figure 4.4: A detail of how the FBG is being glued to a composite structure [23].

Remote Sensing

N. Casagli et al. in [32] present various remote sensing techniques, which are shown in Figure 4.5. These techniques utilize electromagnetic waves to sense soil movements from distance that can range from a few meters to kilometers in the case of satellite remote sensing.
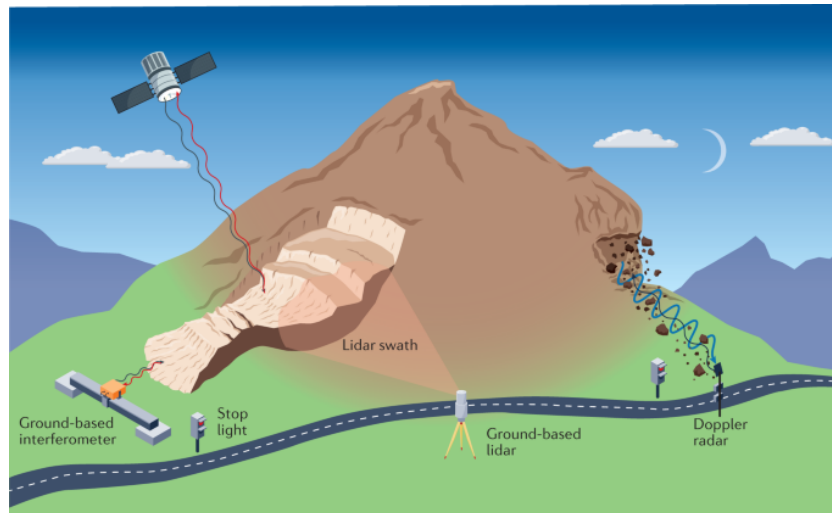
Figure 4.5: An overview of various remote sensing techniques for landslide detection. Adapted from [32].

Among the most popular remote sensing techniques for landslide monitoring are ground- or satellite-based interferometric methods, LiDARs, or Doppler radar techniques. Figure 4.6 presents the measurement capabilities that these techniques provide [32].

However, such techniques focus on the displacement of the slope and are not able to obtain information about processes within the soil. This makes prediction of landslides a very challenging task.

4.2   Landslide Detection Processing

Having detected or predicted an FBG signal allows one to assign the wavelength shift to a certain applied strain on the FBG within the soil. However, for the detection of a landslide, we also need to know the behavior of the soil when such stress is present. The graph in Figure 4.7 shows an idealized model of the strain-stress curve.

As shown in [34], the strain-stress characteristic contains elastic and plastic regions. Within the elastic region, the resulting stress σ_{stress} is proportional

Figure 4.6: Comparison of the measurement properties of the state of the art remote sensing techniques. Adapted from [32].
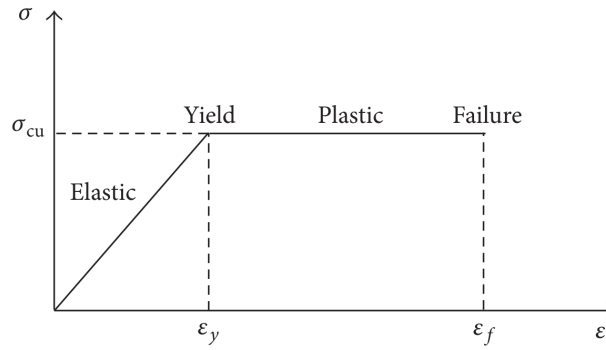
Figure 4.7: Ideal model of dependence of stress on the applied strain. Adapted from [33].

to the applied strain ε defined by Hooke's law as

$$\sigma_{\text{stress}} = E\varepsilon, \tag{4.1}$$

where E represents Young's modulus of elasticity. Such changes are temporal, hence once we stop applying strain, the material returns to its original form. However, when we exceed the critical strain ε_γ, we enter the plastic region of the characteristics, during which permanent changes occur within the material. In landslide monitoring, this results in the beginning of soil movements.

For SHM with FBG sensors we have to focus on the elastic region of the strain-stress characteristics. Knowing that a certain strain $\varepsilon < \varepsilon_\gamma$ is applied, we can develop an early-warning system that would alarm when such a strain is reached.

4.3 Proposed Approach and Topology to Landslide Monitoring

For my measurements of landslide monitoring, I decided to use FBGs embedded within composite structures. To the best of my knowledge, such sensors have not yet been deployed in a slope monitoring experiments. In this thesis I focused on research of two scenarios – (i) landslide detection and (ii) long-term monitoring of a slope.

4.3.1 Landslide-Detecting Case

For the case of landslide detection, I performed two measurements on an artificial slope with artificial rain at the Faculty of Civil Engineering, presented in Figure 4.8. The setup consisted of two embedded FBGs and a pressure sensor installed within the soil. The upper three meters of the container were filled with sand, while the bottom one meter was left empty. Two composite-embedded FBGs were installed into the slope, one at the air-sand interface, while the second one was placed to the upper one meter of the slope. A pressure sensor was also installed within the slope, at position one meter above the FBG at air-sand interface.
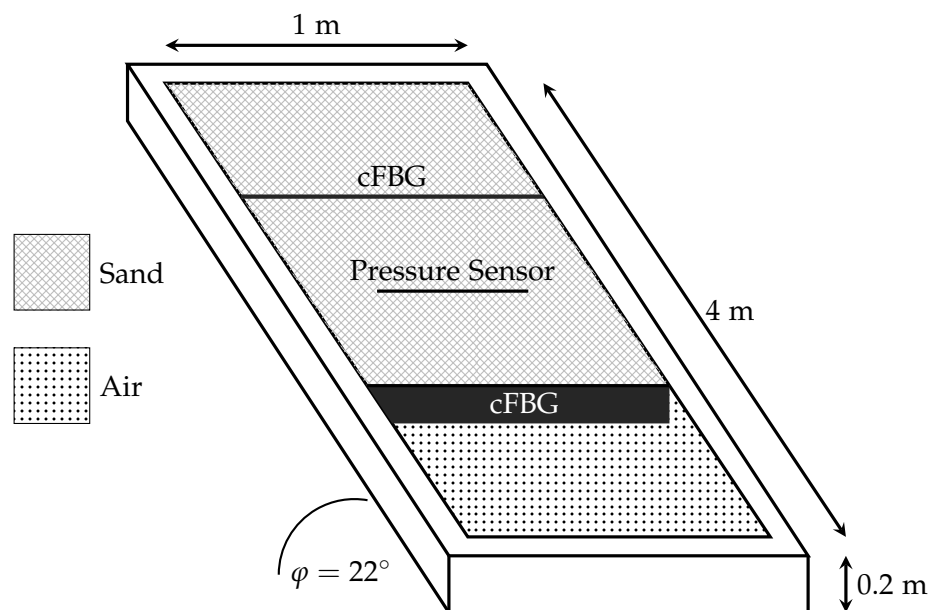
Figure 4.8: Setup of the measurement for force-monitoring during a landslide.

During these measurements, a constant rainfall was set off and was kept on until a landslide occurred.

4.3.2 Long-Term Monitoring Case

Long-term measurements were again conducted on the same artificial slope with artificial rain, with the setup being shown in Figure 4.9. Two composite-embedded FBGs were again used for strain measurement, and an additional embedded FBG was placed at the bottom of the container. Two FBGs were installed for compensation for temperature variations, one within the soil, while the other one was attached to the container frame. A bare FBG was pre-stretched in the container to detect soil movements.
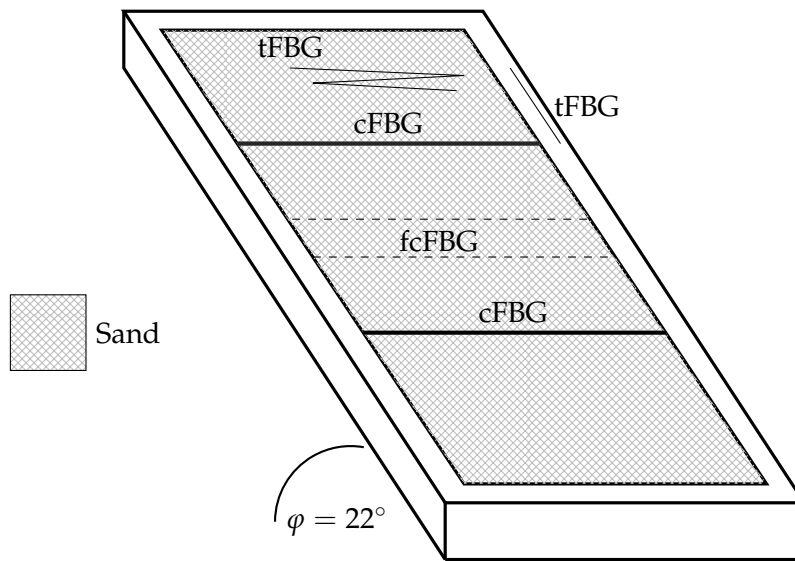
Figure 4.9: Setup of the measurement for long-term monitoring of a slope.

Table 4.1: Types of used FBGs within the slope for landslide detection and long-term monitoring.

Abbreviation	Meaning	Bragg wavelength (nm) [@25°C]
cFBG	Composite Embedded FBG	1548.063 1547.832
tFBG	Temperature-compensating FBG	1548.177 1547.968
fcFBG	Flat lying cFBG	1548.640

Unlike in the landslide scenario, here the rainfall was set off only for limited duration, so that a landslide does not occur, which would ruin the measurement. In this way, we should be able to monitor long-term dependencies within the signals obtained from the FBGs.

Chapter 5

Measurement Results

During the measurements I used an FBG interrogator manufactured by the NETWORK group[1]. This unit was able to obtain the data with a resolution of 0.1 pm with a sampling period of 3.5 seconds on four FBGs, with the interrogator operating in C-band within a 7 nm range. Additionally, a switch could be connected to it, splitting each channel into four, thus providing a 4 to 16 channels split, with acquisition time of 12 seconds per channel. Only FBGs with uniform gratings were used during all measurements conducted. For further analysis of the data, I used the MATLAB.

Figure 5.1: FBG interrogator unit placed on top of the switch.

---

[1]https://sfo.networkgroup.cz/en/interrogation-units/interrogation-unit-for-staticslow-events/

5.1 Bare FBG Analysis

In this section, I discuss measurements of the most common parameters that occur during the deployment of FBG sensor networks for SHM, namely strain and temperature.

5.1.1 Strain

The force affecting the FBG varies depending on the placement of the sensor within the slope. For this reason, two measurements were conducted to examine the response of the FBG to both longitudinal and transverse force.

Longitudinal force

In the case of longitudinal force measurement, the applied strain causes the fiber to stretch in the plane parallel to the fiber, showcased in Figure 5.2. The experimental arrangement involved securing one end of the FBG at a point sufficiently elevated from the ground to ensure that the other end remained airborne. A set of weights up to 217.2 g was then used for attachment to the second end of the fiber, thus applying the longitudinal force to the fiber.
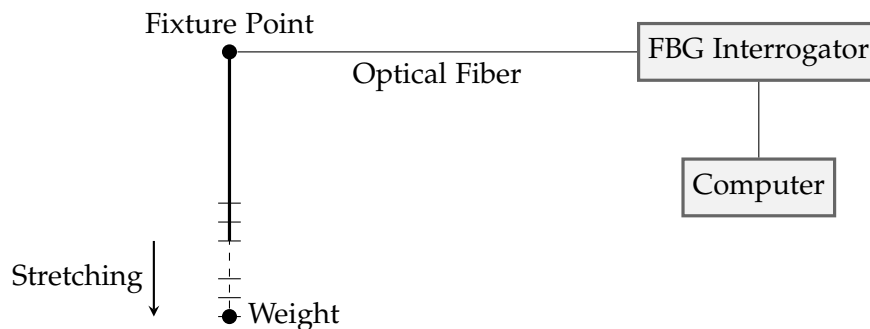
Figure 5.2: Stretching of the FBG due to the applied longitudinal being suspended to it.

The results of this measurement are presented in Figure 5.3, showing a strong linear response that complies with theory, as the measured shift of the wavelength was 13.3 pm/g, which is also the value mentioned in [8].
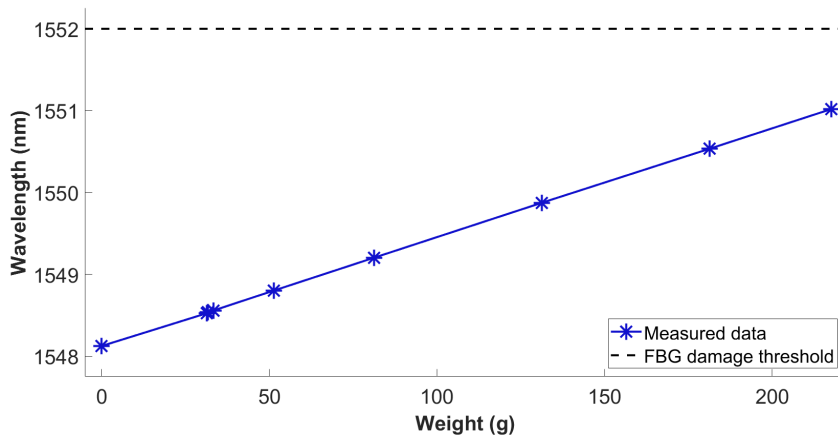
Figure 5.3: Effect of applied longitudinal force on FBG.

Transverse force

The following FBG strain measurement researched the effect of applied transverse force on the FBG. Figure 5.4 showcases the measurement setup, and Figure 5.5 presents a photo of this measurement in the laboratory.
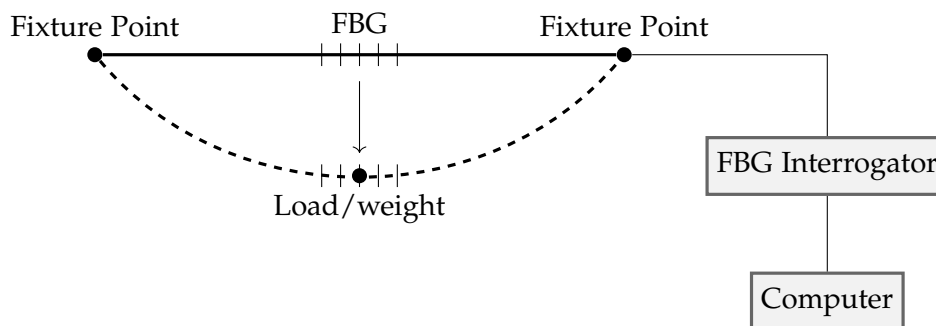
Figure 5.4: Bending of the FBG due to the applied transverse load.

The first setup had the FBG placed in the middle between the two fixed points of the fiber. During this measurement, the weights were placed either directly on the FBG or to a position 10 cm from one of the fixed points. The results of this measurement are shown in Figure 5.6.

This measurement indicated that the force at non-central position caused significantly lower wavelength shift than the central on, with the difference in maximum possible load being 30 grams.
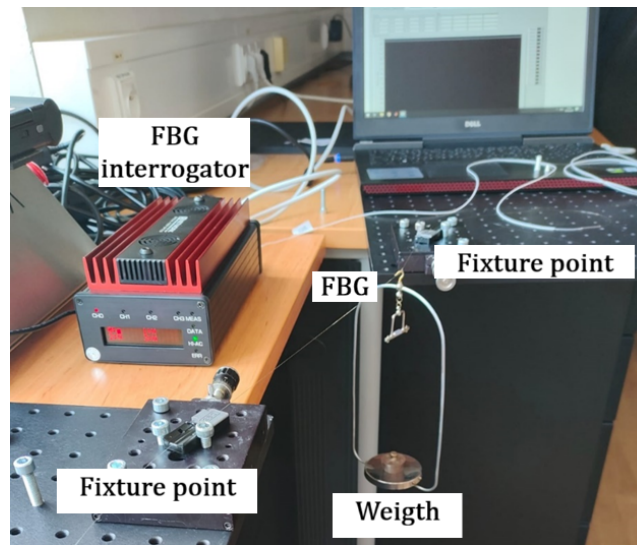
Figure 5.5: Setup used during measurements of transverse force.
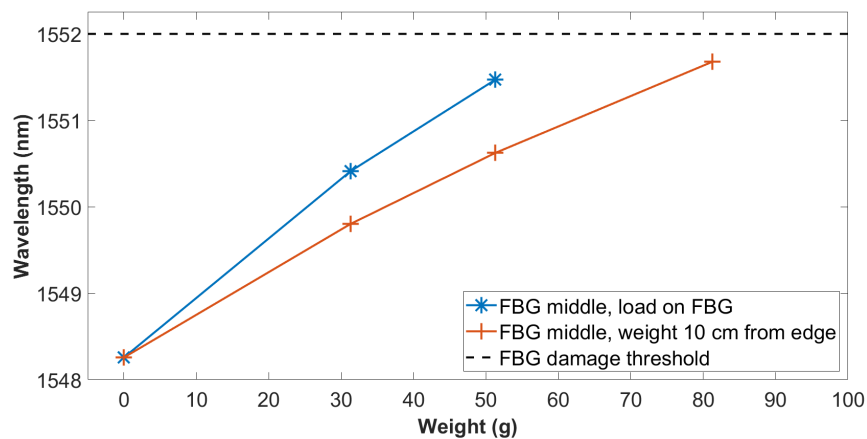
Figure 5.6: Effect of positioning of transverse force on FBG.

The next experiment investigated the influence of the position of the FBG between the fixture points. For that, we used three different positions, where the FBG was placed – in the middle between the fixed points and then 10 and 8 cm from one of the fixed points. The results are presented in Figure 5.7.

The results showed notable difference among the differently positioned fibers, however to distinguish whether this response is based on the positioning of the FBG or on the positiong of the applied force, another measurement has to be conducted. Here it was analyzed how a displaced FBG from the middle is affected by a force of various positioning. The results of this measurement are shown in Figure 5.8.
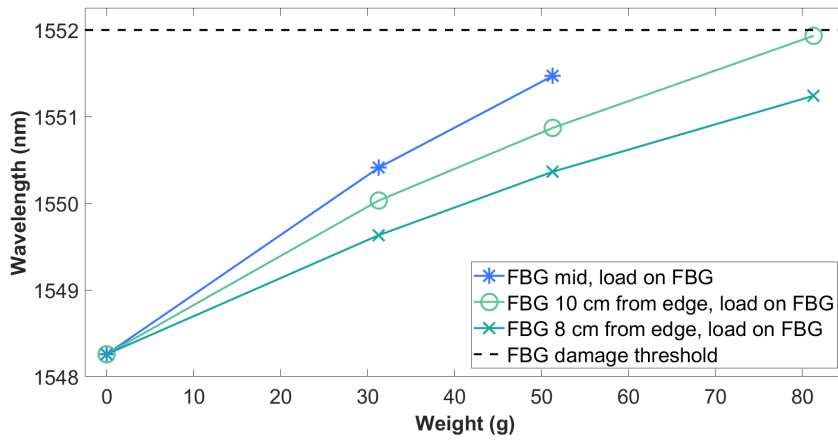
Figure 5.7: Effect of positioning of FBG among the fixture points with transverse force applying directly on the FBGs.
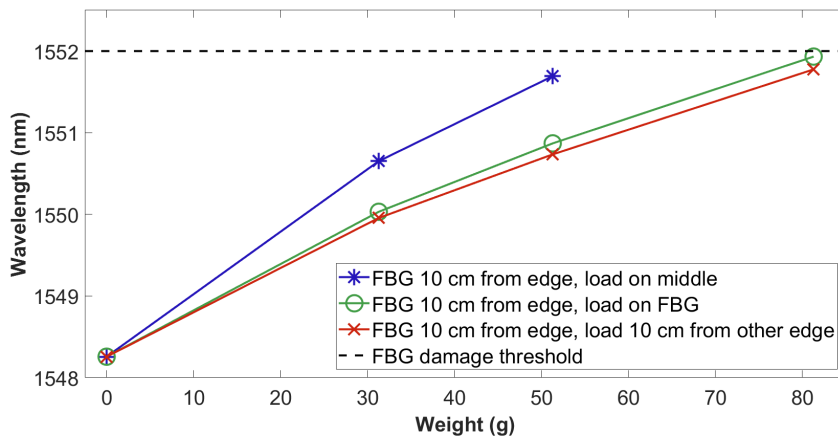
Figure 5.8: Effect of position of force on FBG sensor with non-central placement.

The results of this measurement indicate that the wavelength shift is significantly affected by the position of the applied force. The position of the FBG between the fixture points does not change the response of the FBG to the force, as the results of this measurement are identical to those obtained from the measurement with centrally positioned FBG.

5.1.2 Temperature

To distinguish the wavelength shift caused by the applied strain from the shift that is a result of temperature changes, we need to compensate for the effect of the temperature. This is possible with a setup that has two FBGs where one of them is not affected by the strain and thus can be used for the temperature compensation. To experimentally verify this possibility, we performed a measurement in which two FBGs were installed in a cooling unit, where one of the FBGs was under constant load. The setup within a thermal chamber is shown in Figure 5.9.
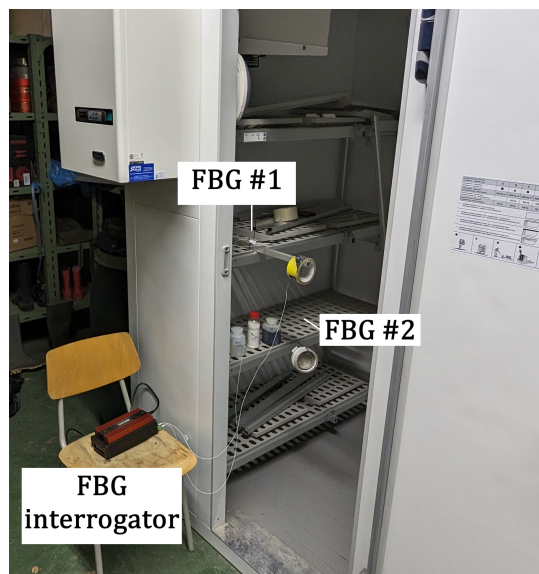
Figure 5.9: The setup used for the measurement of the effects of temperature changes.

During the experiment, the temperature in the unit was changed by steps of 5°C, from 25°C down to 10°C. In Figure 5.11 we can see how the wavelength λ_0 is changed as a result of a sudden change in temperature in the cooling unit.
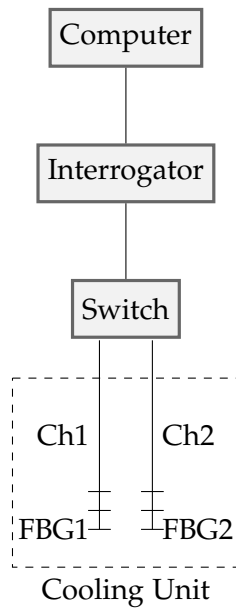
Figure 5.10: The block scheme for the measurement of the effects of temperature changes.
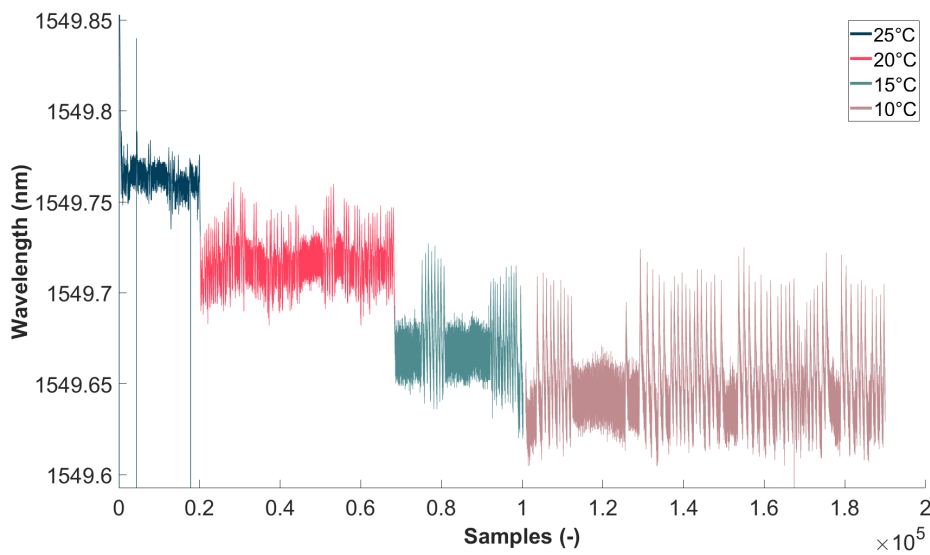
Figure 5.11: Measured effect of temperature on the FBG sensors.

From Figure 5.11 we can observe periodic spikes that appear especially during the lower temperatures at around 10°C. This was probably caused by the imperfection of the cooling unit, where the cooling process stopped after achieving the desired temperature. After that, the temperature in the unit started to rise until the feedback mechanism of the unit started the cooling process again. A detail of this effect is presented in Figure 5.12.
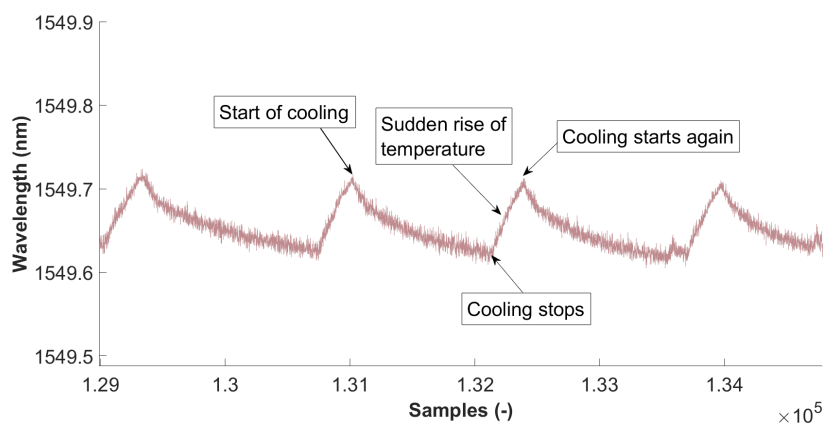
Figure 5.12: Detail of spiking of the wavelength shift caused by imperfect cooling in the unit.

5.2 Embedded FBG Analysis

As presented in the previous section, the maximum load that could be applied to the FBG was maximally hundreds of grams. However, in the landslide-monitoring scenario, we can face loads much higher, and thus there is a need for higher susceptibility of the FBG. This is possible by embedding the FBG into another material, such as carbon or fiberglass composite. This was done in a manner similar to that presented in [26], where the FBG was placed between the carbon layers.

Given the toughness and elasticity of a material that is used for FBG embedding, the response changes accordingly to these parameters, copying the structure's changes like stretching or compression.

During landslide monitoring, we often rather detect soil displacement than forces within the slope. This can be sensed by the bending of the composite structure with the embedded FBG. In order to determine its bending capability, a measurement was performed in which a load was applied on top of the composite structure. We then observed the wavelength change as a response to a given bending. The setup of this experiment is shown in Figure 5.13.

During the measurements, the embedded FBGs were placed on top of a plastic board to reduce its bending. The reason for this is the fact that when such a composite structure is placed within a slope, it will be supported by the surrounding soil.

The graphs in Figure 5.14 show that the embedded FBGs retain their linear response to the applied force, which is demonstrated in this case by bending.
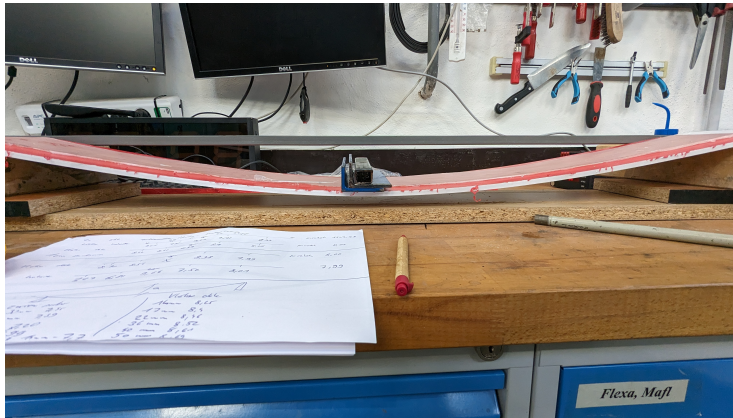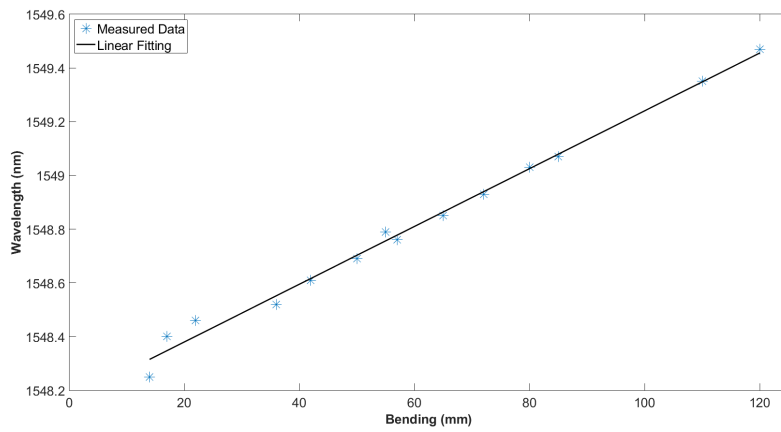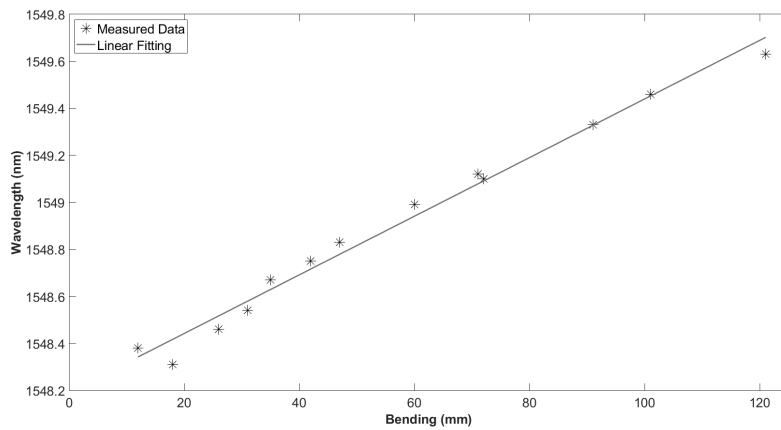
Figure 5.13: Testing of the bending capabilities of the embedded FBGs.

(a) Glass embedded FBG

(b) Carbon embedded FBG

Figure 5.14: Demonstration of the bending capabilities of two differently manufactured composite structures for FBG embedding.

5.3 Slope Monitoring with FBGs

Knowing the maximum bending capabilities of the embedded FBG, I proceeded to tests regarding the landslide monitoring at the Faculty of Civil Engineering, which was presented in the previous chapter. To simplify the tests, sand was used instead of soil, due to its greater susceptibility to landslides. The experiment consisted of artificial rainfall on the slope with sensors. In Figure 5.15 we can see a detail of the container before and after the rain-induced landslide.
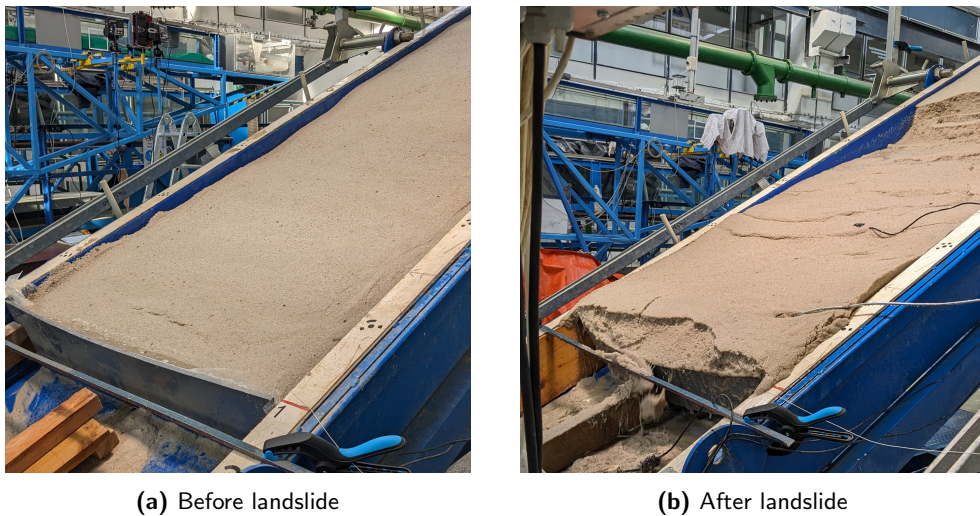

(a) Before landslide   **(b)** After landslide

Figure 5.15: Container filled with sand used during the landslide monitoring measurement.

During the initial measurement, one of the FBGs experienced a negative wavelength shift because of the orientation of the composite placed within the slope. This caused the peak to shift away from the spectral range of the FBG interrogator. The response of the other FBG sensor within the soil is presented in Figure 5.16. We can observe that the curve is similar to the idealized strain-stress characteristics, making it suitable for slope stability monitoring.

Figure 5.17 presents the measured response during the landslide by the FBG in comparison with the pressure sensor data. Both signals clearly show a spike when a landslide occurs, followed by a sudden drop, as a result of the flow of the surrounding sand, effectively releasing the pressure off the sensors. In this case, we can see that the FBG data more clearly show the transition between elastic and plastic regions.
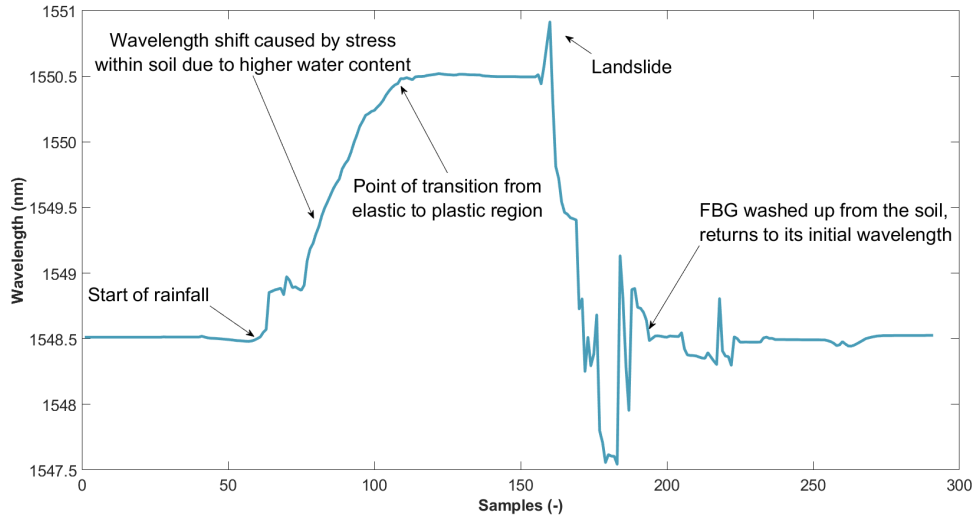
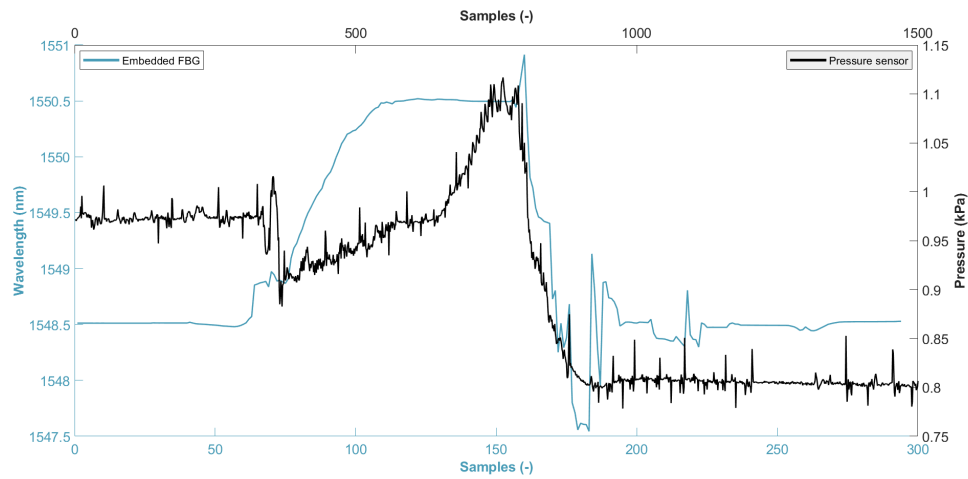**Figure 5.16:** Measured wavelength shift as a response to the soil movement.

Figure 5.17: Comparison of the data acquired by the FBG and the data obtained by the pressure sensor.

5.4 Long-Term Slope Monitoring

The long-term monitoring took place over a span of 20 days, where the data was collected by six FBGs simultaneously, as presented in the previous chapter. The signals of the FBGs monitoring the temperature variations are presented in Figure 5.18, while the strain-sensing signals of embedded FBGs are shown in Figure 5.19.
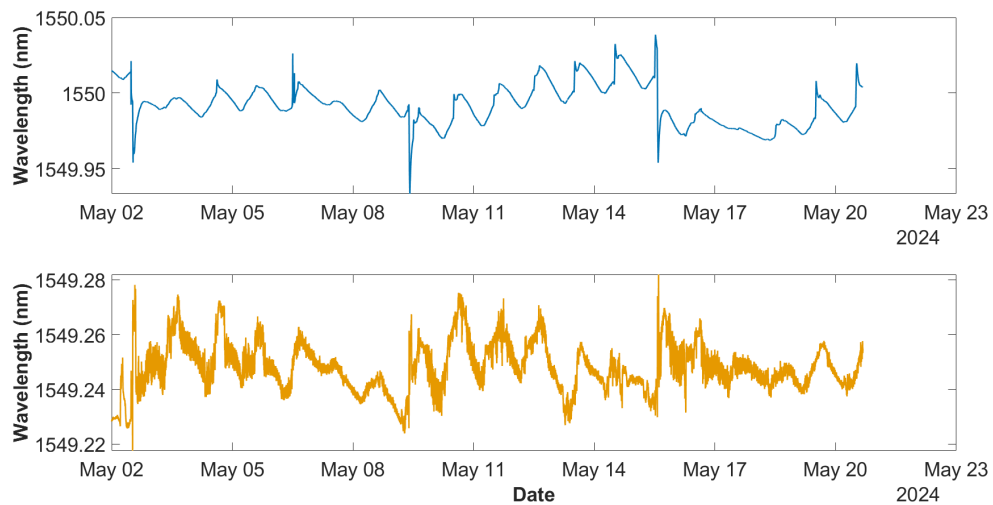

Figure 5.18: Monitoring of temperature variations – signal of FBG within soil (top), signal of FBG attached to the container outside of the soil (bottom).

We can observe that the data of the FBG attached to the construction of the container, is significantly more noisy, compared to the one obtained from within the soil. This is a result of direct sunlight affecting the outer FBG, inducing changes that are not present within the soil mass, and therefore in this case act as a noise.

From the strain data, we can see that the temperature variations are also noticeable, as these signals have not been compensated for such changes. The data clearly shows how the response changed as a result of setting the slope from an initial 0° to 22° on May 7. During May 9 and May 15 a rainfall was set off, where a detail of one of these changes is presented in Figure 5.20.

The rainfall, which was present for duration of 30 minutes, induced changes within the soil that lasted for about an hour. After that the water content got probably to similar level as before the rain, as the signals then returned to their initial wavelengths.
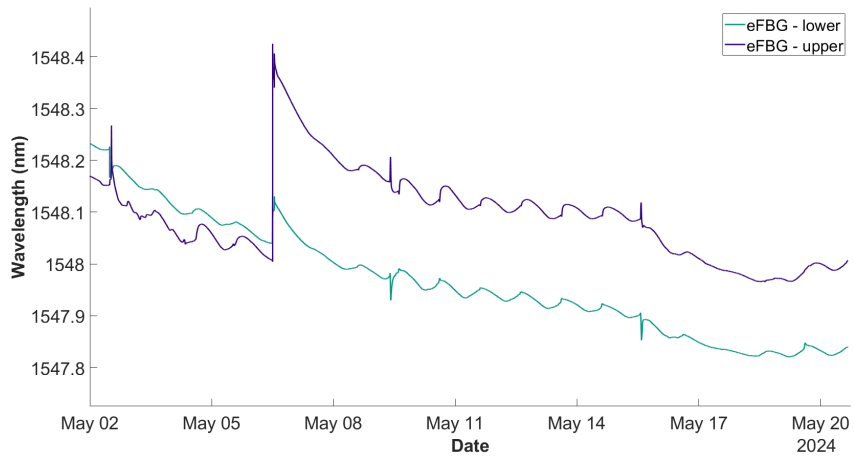
Figure 5.19: Monitoring of strain within the slope during long-term measurement with embedded FBGs being placed in upper or lower part of the slope.
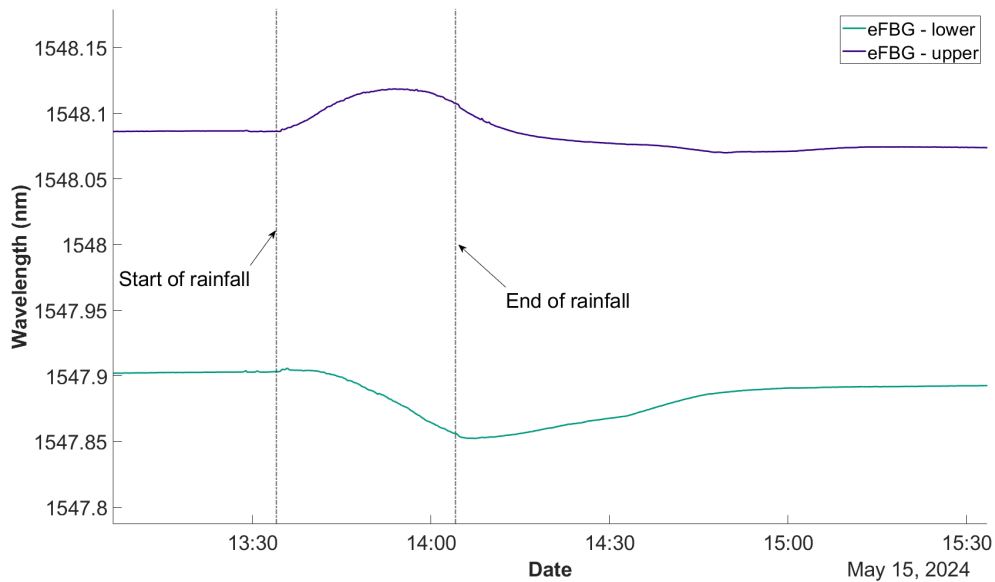

Figure 5.20: Rainfall-induced wavelength shift on May 15.

Chapter 6

Experimental Data Evaluation

In this chapter, I present how the data obtained during the measurements in Chapter 5 can be processed, showcasing temperature-compensation and landslide detection algorithms. Furthermore, I present ANN-based prediction system, which was trained using data from the long-term measurement of the previous chapter.

6.1 Preprocessing of the Data

Compensation for temperature variations plays a significant role in the FBG data preprocessing. A measurement regarding temperature sensing was presented in the previous chapter, where two FBGs were installed to a cooling unit. The temperature compensation was then performed by subtracting the variation of one signal from the other signal. The resultant temperature-compensated signal is shown in Figure 6.1.
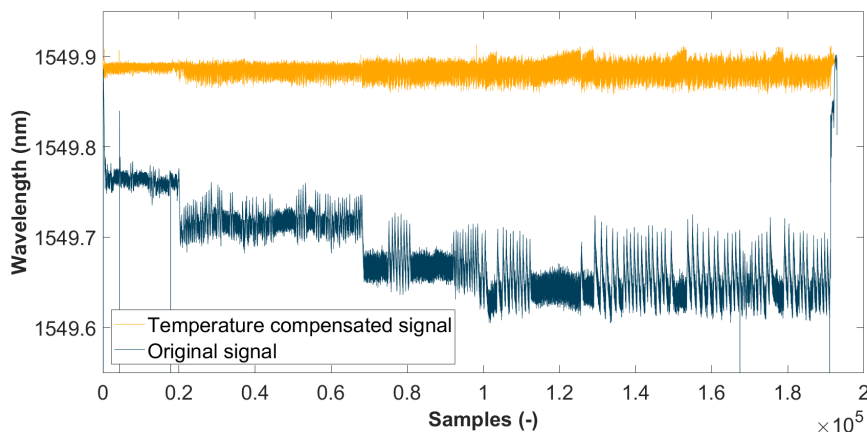

Figure 6.1: Comparison of the original and temperature-compensated signal.

For detection of the landslide collision state I decided to use a simple thresholding method. Recalling the acquired response during the rainfall on the slope from the previous chapter, we focus on the part within the elastic region, as landslides occur once the transition between the elastic and plastic regions takes place. I decided to set the threshold to a level of 80 % of wavelength shift, where at 100 % a landslide would occur.
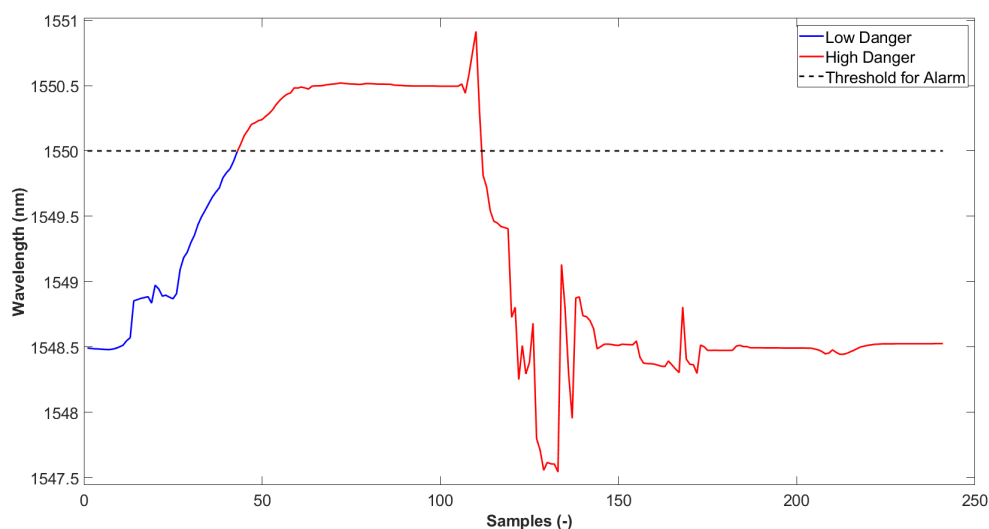

Figure 6.2: Thresholding method for early-warning system for possible landslide.

6.2 ANN-based Prediction

Signal prediction plays important part in modern early-warning system. However, ANNs rely on large amounts of data that are used for training of such networks. For that reason, I decided to train an ANN for a prediction of temperature signal of an FBG, as I had access to such data collected over a span of 10 days.

The available data consisted of 114570 samples, which were roughly divided in a 70:10:20 ratio into train, validation, and test sets, respectively. The goal of the prediction task was to forecast the next 10 samples (corresponding to two minutes) of the data based on a given number of previous samples. Normalization of the data was performed before the training by subtracting the mean and division by the standard deviation, to enhance generalization of the ANN.

The network used is presented in Figure 6.3, and consisted of two hidden layers, namely LSTM and fully connected layer. The reasoning behind the choice of the layers was that we want to develop a light-weight system

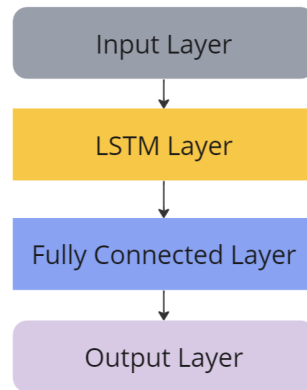capable of predictions, and therefore I decided to limit the hidden layers to just those presented beforehand.

Figure 6.3: Layers of the used ANN for temperature signal forecasting.

As a solver for the ANN I used adaptive moment estimation (ADAM), with the maximum number of epochs being set to 120, with the possibility of early stopping, where validation would be calculated every third epoch. The validation patience, during which we wait whether the validation loss does not decrease and after which we stop the training process, was set to four. The initial learning rate η was set to 10^{-3}.

To acquire optimal hyperparameters, I performed a grid search among the number of hidden parameters of LSTM, and the length of a sequence of data on which the prediction would be based. The reason why I chose these hyperparameters is that they both contribute to the final complexity of the purposed model, and therefore I wanted to research their optimal values. To limit the fluctuations of the results, caused by the randomness of the initial weights within the network, I trained each network three separate times, and the final result was set as the average of these results. The heatmap with the results is presented in Figure 6.4, where the color of the cells denotes the root mean square error (RMSE) on the validation set for a given hyperparameter pair.

From the heatmap, we can observe that the best performing model is ANN with 110 hidden units, which takes 75 samples as a basis for its prediction. From the results, we can clearly see a trend denoting a lower RMSE with a higher number of hidden layers. This was expected, as hidden layers determine the complexity of the system, and thus they should be able to predict data more accurately.

Another trend in the results indicates that longer sequences used for the prediction lead to higher RMSE. This suggests that these models are not able to pick up on patterns within the longer sequences, which causes them to
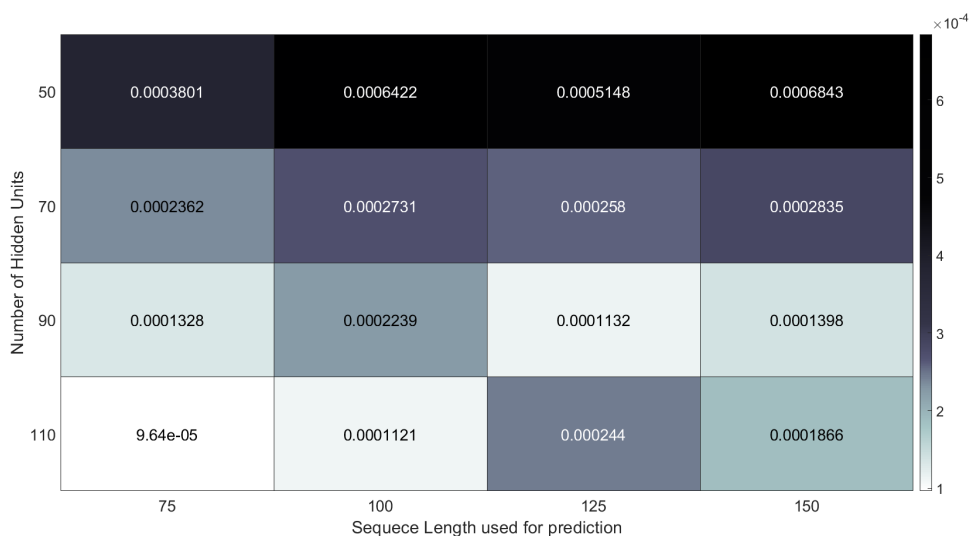
Figure 6.4: Heatmap showcasing the RMSE values obtained for given pair of hyperparameters.

provide worse forecasts compared to models with shorter sequence lengths. This might be related to the processes within the soil, and would be worth studying in depth in future work in a real-case scenario.

As the final model I have chosen the network with 90 hidden units and the sequence length for prediction of 75. The reason for this choice is that while not being the best model, the complexity of the task is not that high, and therefore I think the results of this network with given number of hidden parameters are sufficient. I also chose the model that uses 75 samples rather than the one that uses 125 samples for basis of the prediction, as the trend showed better performance of networks that used shorter sequences.

The prediction made on the test set by the final model is shown in Figure 6.5, and Figure 6.6 presents the error of the prediction. We can see that the maximum error for the prediction is 4.3 pm, which was present due to an imperfect peak estimate.

The key metrics for the final model are RMSE and mean absolute error (MAE). The calculated RMSE on the test set is 0.30 pm, suggesting that on average the predicted values are off by this value. The MAE value was 0.17 pm, indicating the average error made by the prediction on the test set. From these results, we can see that the forecasting capability is very reasonable, where both RMSE and MAE values being near the resolution of the FBG interrogator.
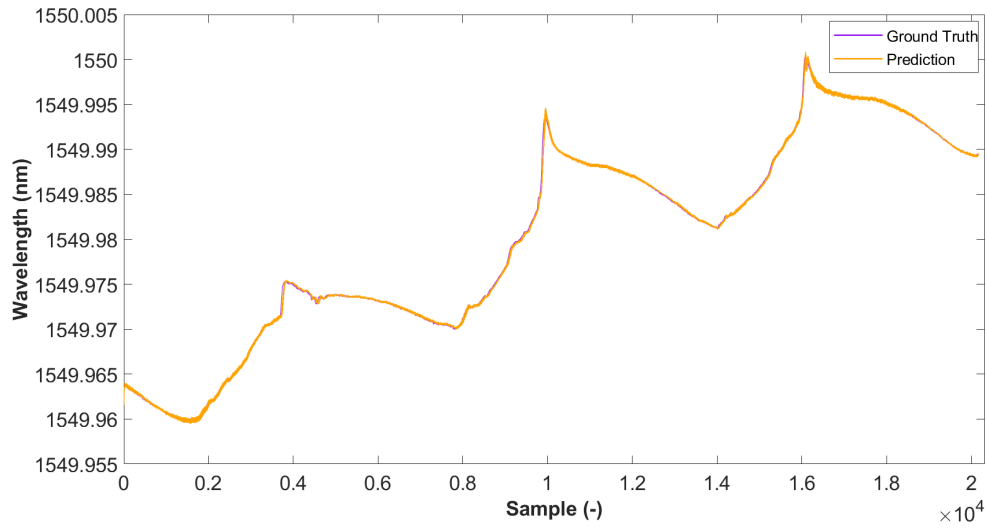
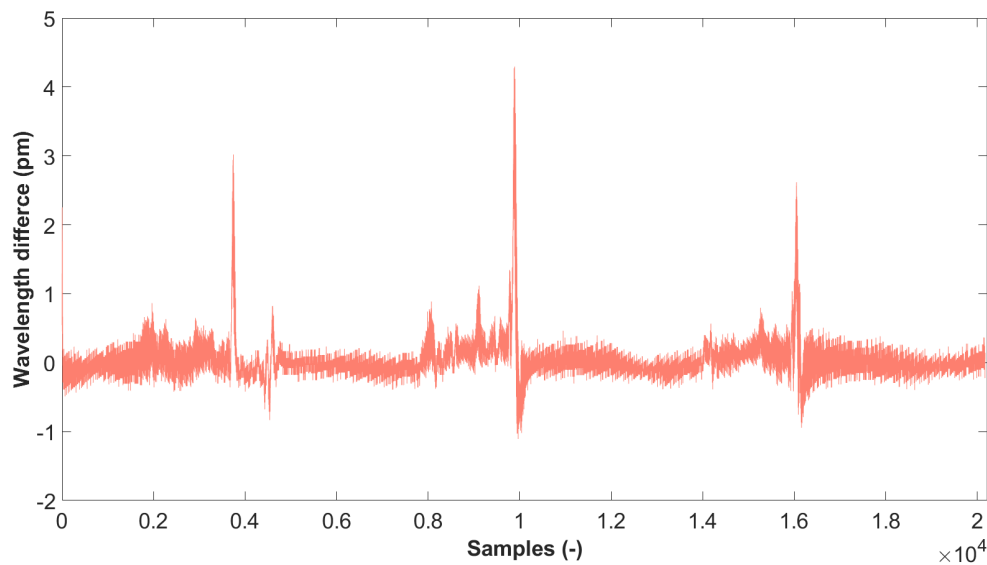**Figure 6.5:** Comparison of the prediction made by the final model and the ground truth of the test set.

Figure 6.6: The difference calculated between the ground truth and the prediction of the final model on the test set.

Chapter 7

Conclusion

In this thesis I presented the working principles behind FBG sensors with a focus on the SHM purposes. FBGs with various gratings were discussed, as well as the response of the uniform grating FBG to applied external phenomena. I further discussed the manufacturing techniques for FBG fabrication and the FBG-based sensor networks and their topologies.

Afterwards, signal processing techniques were presented. The peak detection from the reflected spectrum by the FBG was presented, showcasing both the direct techniques that estimate the peak from the obtained spectrum and the fitting methods that use curves to approximate the shape of the peak. I then discussed the compensation of ambient effects that might disrupt the FBG sensor measurements, with a focus mainly being put on temperature compensation. I then presented ANNs with their inner composition and training techniques. LSTM cells were introduced as a suitable component of ANNs when dealing with long-term dependencies.

Chapter 4 presented the setups for the following measurements, discussing the approaches for landslide detection and long-term measurements. During the experiments performed, the effect of both transversal and longitudinal forces on the FBG was researched. The results showed a significant difference among these measurements, where the fiber exhibited significantly larger durability during the longitudinal measurement. I then proceeded to measurements with composite embedded FBGs that were first classified in terms of their bending capabilities. After that, these FBGs were inserted into an artificial slope. Two measurements were performed with this slope, researching the forces applied to the FBG during a landslide, and the a measurement monitoring long-term dependencies within the sand slope.

The acquired data from the long-term measurement were then used for the training of an ANN for temperature signal forecasting. To obtain ideal hyperparameter values, a grid search was performed, tuning the number

of hidden layers and the sequence length used for prediction. The final model, which was selected, had 90 hidden units, where such a network was capable of predicting the next 10 samples based on the previous 75 samples, providing forecasting information for the next two minutes. The metrics calculated on the test set were RMSE with a value of 0.30 pm and MAE of 0.17 pm, suggesting that this network is capable of very precise forecasting, where the error is near the resolution of the FBG interrogator.

Bibliography

[1] R. Hui and M. O'Sullivan, *Fiber Optic Measurement Techniques*. Burlington, United States of America: Academic Press, Dec. 2008, ISBN: 978-0-12-373865-3.

[2] R. Kashyap, *Fiber Bragg gratings*, 2nd ed. San Diego, United States of America: Academic Press, Nov. 2009, ISBN: 978-0-12-372579-0.

[3] J. D. Joannopoulos *et al.*, *Photonic crystals: Molding the flow of light*. Princeton, United States of America: Princeton University Press, 2008, ISBN: 978-0-691-12456-8.

[4] J. Zhao *et al.*, "Calculation of photonic band-gap of one dimensional photonic crystal," *Journal of Physics: Conference Series*, vol. 183, p. 012 018, Aug. 2009, ISSN: 1742-6596. DOI: 10.1088/1742-6596/183/1/012018.

[5] K. T. V. Grattan and B. T. Meggitt, *Optical fiber sensor technology: advanced applications – Bragg gratings and distributed sensors*. Dordrecht, The Netherlands: Springer, Sep. 2000, vol. 5, ISBN: 978-0-7923-7946-1.

[6] C. E. Campanella *et al.*, "Fibre bragg grating based strain sensors: Review of technology and applications," *Sensors*, vol. 18, no. 9, p. 3115, Sep. 2018, ISSN: 1424-8220. DOI: 10.3390/s18093115.

[7] D. Kinet *et al.*, "Fiber bragg grating sensors toward structural health monitoring in composite materials: Challenges and solutions," *Sensors*, vol. 14, no. 4, pp. 7394–7419, Apr. 2014, ISSN: 1424-8220. DOI: 10.3390/s140407394.

[8] R. J. Black *et al.*, "On the gage factor for optical fiber grating strain gages," *In Proceedings of the 53rd International SAMPE Symposium and Exhibition (SAMPE 2008)*, vol. 52, Jan. 2008.

[9] M. Fajkus *et al.*, "Design of fiber bragg grating sensor networks," *IEEE Transactions on Instrumentation and Measurement*, vol. 71, pp. 1–11, Nov. 2021, ISSN: 1557-9662. DOI: 10.1109/TIM.2021.3127642.

[10] C. Cuadrado-Laborde, *Current Trends in Short- and Long-period Fiber Gratings*. Rijeka, Croatia: IntechOpen, May 2013, ISBN: 978-953-51-1131-3. DOI: 10.5772/3320.

[11] G. D. Marshall *et al.*, "Point-by-point written fiber-bragg gratings and their application in complex grating designs," *Optics Express*, vol. 18, no. 19, pp. 19 844–19 859, Sep. 2010. DOI: 10.1364/OE.18.019844.

[12] D. Tosi, "Review and analysis of peak tracking techniques for fiber bragg grating sensors," *Sensors*, vol. 17, no. 10, p. 2368, Oct. 2017, ISSN: 1424-8220. DOI: 10.3390/s17102368.

[13] H.-H. Zhu *et al.*, "Investigation of the evolutionary process of a reinforced model slope using a fiber-optic monitoring network," *Engineering Geology*, vol. 186, pp. 34–43, Feb. 2015. DOI: 10.1016/j.enggeo.2014.10.012.

[14] C. Tian *et al.*, "Investigation on peak wavelength tracking in fbg sensor," in *2023 Photonics Global Conference (PGC)*, IEEE, Aug. 2023. DOI: 10.1109/pgc60057.2023.10344288.

[15] I. Goodfellow *et al.*, *Deep Learning*. MIT Press, 2016, http://www.deeplearningbook.org.

[16] Y. LeCun *et al.*, "Deep learning," *Nature*, vol. 521, no. 7553, pp. 436–444, May 2015, ISSN: 1476-4687. DOI: 10.1038/nature14539.

[17] K.-L. Du *et al.*, "Perceptron: Learning, generalization, model selection, fault tolerance, and role in the deep learning era," *Mathematics*, vol. 10, no. 24, p. 4730, Dec. 2022, ISSN: 2227-7390. DOI: 10.3390/math10244730.

[18] Y. Tian *et al.*, "Recent advances in stochastic gradient descent in deep learning," *Mathematics*, vol. 11, no. 3, p. 682, Jan. 2023, ISSN: 2227-7390. DOI: 10.3390/math11030682.

[19] D. P. Kingma and J. L. Ba, *Adam: A method for stochastic optimization*, Dec. 2014. DOI: 10.48550/arXiv.1412.6980.

[20] C. M. Bishop, *Pattern Recognition and Machine Learning*. New York, United States of America: Springer, Aug. 2006, ISBN: 978-0387-31073-2.

[21] Y. Yu *et al.*, "A review of recurrent neural networks: Lstm cells and network architectures," *Neural Computation*, vol. 31, no. 7, pp. 1235–1270, Jul. 2019, ISSN: 1530-888X. DOI: 10.1162/neco_a_01199.

[22] Y. Zhang and X. Song, "Load prediction of space deployable structure based on fbg and lstm," *IEEE Access*, vol. 7, pp. 13 715–13 722, Jan. 2019, ISSN: 2169-3536. DOI: 10.1109/access.2019.2893364.

[23] L. Xiong *et al.*, "Investigation of the temperature compensation of fbgs encapsulated with different methods and subjected to different temperature change rates," *Journal of Lightwave Technology*, vol. 37, no. 3, pp. 917–926, Feb. 2019, ISSN: 1558-2213. DOI: 10.1109/jlt.2018.2883817.

[24] T. Li *et al.*, "Recent advances and tendency in fiber bragg grating-based vibration sensor: A review," *IEEE Sensors Journal*, vol. 20, no. 20, pp. 12074–12087, Oct. 2020, ISSN: 2379-9153. DOI: 10.1109/jsen.2020.3000257.

[25] T. Xiaolin *et al.*, "A miniaturized, low-cost and portable fiber bragg grating interrogation system for remote monitoring," *Optik*, vol. 248, p. 168054, Dec. 2021, ISSN: 0030-4026. DOI: 10.1016/j.ijleo.2021.168054.

[26] M. Gabardi *et al.*, "Embedding fiber bragg grating sensors in carbon composite structures for accurate strain measurement," *IEEE Sensors Journal*, vol. 23, no. 15, pp. 16882–16892, Aug. 2023, ISSN: 2379-9153. DOI: 10.1109/jsen.2023.3285408.

[27] H. Pei *et al.*, "Slope stability analysis based on real-time displacement measurements," *Measurement*, vol. 131, pp. 686–693, Jan. 2019, ISSN: 0263-2241. DOI: 10.1016/j.measurement.2018.09.019.

[28] M. S. M. Sa'ad *et al.*, "A fiber bragg grating-based inclinometer probe with enhanced sensitivity for a higher slope profiling resolution," *Sensors and Actuators A: Physical*, vol. 364, p. 114804, Dec. 2023, ISSN: 0924-4247. DOI: 10.1016/j.sna.2023.114804.

[29] L. Zhang *et al.*, "An fiber bragg grating-based monitoring system for slope deformation studies in geotechnical centrifuges," *Sensors*, vol. 19, no. 7, p. 1591, Apr. 2019, ISSN: 1424-8220. DOI: 10.3390/s19071591.

[30] H.-L. Liu *et al.*, "Experimental study on an fbg strain sensor," *Optical Fiber Technology*, vol. 40, pp. 144–151, Jan. 2018, ISSN: 1068-5200. DOI: 10.1016/j.yofte.2017.09.003.

[31] M. Yeager *et al.*, "Assessment of embedded fiber bragg gratings for structural health monitoring of composites," *Structural Health Monitoring*, vol. 16, no. 3, pp. 262–275, Aug. 2016, ISSN: 1741-3168. DOI: 10.1177/1475921716665563.

[32] N. Casagli *et al.*, "Landslide detection, monitoring and prediction with remote-sensing techniques," *Nature Reviews Earth & Environment*, vol. 4, no. 1, pp. 51–64, Jan. 2023, ISSN: 2662-138X. DOI: 10.1038/s43017-022-00373-x.

[33]   J. Xin *et al.*, "Analysis of tensile strength's influence on limit height and active earth pressure of slope based on ultimate strain method," *Advances in Materials Science and Engineering*, vol. 2017, pp. 1–8, 2017, ISSN: 1687-8442. DOI: 10.1155/2017/6824146.

[34]   W. D. Callister Jr. and D. G. Rethwisch, *Materials science and engineering: An introduction*, 10th ed. Hoboken, United States of America, Nov. 2017, ISBN: 9781119405405.